

¹⁸²W and HSE constraints from 2.7 Ga komatiites on the heterogeneous nature of the Archean mantle

Igor S. Puchtel^{1*}, Janne Blichert-Toft², Mathieu Touboul^{1,2}, and Richard J. Walker¹

¹Department of Geology, University of Maryland, College Park, MD 20742, USA

²Laboratoire de Géologie de Lyon, Ecole Normale Supérieure de Lyon and Université Claude Bernard Lyon 1,
CNRS UMR 5276, 46 Allée d'Italie, 69007 Lyon, France

*Corresponding author: ipuchtel@umd.edu

Revised for:

Geochimica et Cosmochimica Acta

Version: Final Revision

Keywords: ^{182}Hf - ^{182}W and ^{187}Re - ^{187}Os isotopic systems, deficit in highly siderophile elements, Boston Creek komatiitic basalt lava flow, stochastic late accretion, sluggish mixing of the mantle

36 **Abstract**

37 While the isotopically heterogeneous nature of the terrestrial mantle has long been
38 established, the origin, scale, and longevity of the heterogeneities with regard to different
39 elements and isotopic systems are still debated. In this study, we report Nd, Hf, W, and Os
40 isotopic and highly siderophile element (HSE) abundance data for the Boston Creek
41 komatiitic basalt lava flow (BCF) in the 2.7 Ga Abitibi greenstone belt, Canada. This lava
42 flow is characterized by strong depletions in Al and heavy rare earth elements (REE),
43 enrichments in light REE, and initial $\epsilon^{143}\text{Nd} = +2.5 \pm 0.2$ and $\epsilon^{176}\text{Hf} = +4.2 \pm 0.9$ indicative of
44 derivation from a deep mantle source with time-integrated suprachondritic Sm/Nd and Lu/Hf
45 ratios. The data plot on the terrestrial Nd-Hf array suggesting minimal involvement of early
46 magma ocean processes in the fractionation of lithophile trace elements in the mantle source.
47 This conclusion is supported by a mean $^{142}\text{Nd}/^{144}\text{Nd}$ that is unresolvable from terrestrial
48 standards. At the same time, the BCF exhibits a positive ^{182}W anomaly ($\mu^{182}\text{W} = +11.7 \pm 4.5$),
49 yet is characterized by chondritic initial $\gamma^{187}\text{Os} = +0.1 \pm 0.3$ and low HSE abundances inferred
50 for its mantle source ($35 \pm 5\%$ of those estimated for the present-day Bulk Silicate Earth, BSE).
51 Collectively, these characteristics are unique among the Archean komatiite systems studied so
52 far. The deficit in the HSE, coupled with the chondritic Os isotopic composition, but a
53 positive ^{182}W anomaly, are best explained by derivation of the parental BCF magma from a
54 mantle domain characterized by predominance of HSE-deficient, differentiated late accreted
55 material. According to the model presented here, the mantle domain that gave rise to the BCF
56 received only $\sim 35\%$ of the present-day HSE complement in the BSE before becoming
57 isolated from the rest of the convecting mantle until the time of komatiite emplacement at
58 2.72 Ga. These new data provide strong evidence for the highly heterogeneous nature of the
59 Archean mantle in terms of absolute HSE abundances and for its slow mixing, on a time scale
60 of at least 1.7 billion years. Additionally, they are consistent with a stagnant-lid plate tectonic
61 regime in the Hadean and Archean, prior to the onset of modern-style plate tectonics.

62

63 **1. Introduction**

64 While the isotopically heterogeneous nature of the terrestrial mantle has long been
65 established, the origin, scale, and longevity of the heterogeneities with regard to different
66 elements and isotopic systems are still debated. Some of the chemical heterogeneities may
67 have been primordial, reflecting planetary accretion/differentiation and magma ocean
68 crystallization processes, whereas others have definitively resulted from later processes
69 associated with the dynamic regime of the planet, especially crustal recycling. The ^{142}Nd and
70 ^{182}W anomalies found in some early Earth rocks likely formed within the first \sim 500 and \sim 50
71 Ma, respectively, of Earth's history, while ^{146}Sm and ^{182}Hf were still extant, as a result of
72 early planetary differentiation event(s). The largest ^{142}Nd anomalies, ranging as high as +20
73 ppm and as low as -15 ppm, have been reported for the Eoarchean or older supracrustal rocks
74 from the Isua greenstone belt, Greenland (Boyett *et al.*, 2003; Caro *et al.*, 2003; Boyett and
75 Carlson, 2005; Boyett and Carlson, 2006; Caro *et al.*, 2006; Bennett *et al.*, 2007; Rizo *et al.*,
76 2011; Rizo *et al.*, 2012; Rizo *et al.*, 2013), the Nuvvuagittuq greenstone belt, Québec (O'Neil
77 *et al.*, 2008; O'Neil *et al.*, 2012; Roth *et al.*, 2013), and the Ukaliq supracrustal belt, Québec
78 (Caro *et al.*, 2017). Few terrestrial samples younger than 3.5 Ga are known to have $\mu^{142}\text{Nd}$
79 values deviating from terrestrial standards by more than ± 3 ppm (Rizo *et al.*, 2012; Debaille
80 *et al.*, 2013). Similarly, positive ^{182}W anomalies as high as +23 ppm have been reported for
81 supracrustal rocks from Greenland and Québec (Willbold *et al.*, 2011; Touboul *et al.*, 2014;
82 Dale *et al.*, 2017), as well as from the Northwest Territories (Willbold *et al.*, 2015) and
83 Fennoscandia (Puchtel *et al.*, 2016b).

84 The apparent disappearance of ^{142}Nd anomalies during the Archean was initially
85 interpreted as evidence for re-homogenization of early-formed silicate reservoirs within the
86 mantle on the time scale of at least one billion years (Caro *et al.*, 2006; Bennett *et al.*, 2007;
87 Carlson and Boyett, 2008). The presence of sizeable isotopic anomalies in late Archean and

88 younger rocks, however, indicates that mantle mixing did not completely eliminate primordial
89 anomalies early in Earth history. The ~15 ppm positive ^{182}W anomalies found in the 2.82 Ga
90 Kostomuksha komatiites were interpreted to indicate that early-formed domains in the mantle
91 survived for at least 1.7 Ga (Touboul *et al.*, 2012), while ^{182}W isotopic heterogeneities in the
92 Phanerozoic, including modern rocks from Baffin Bay, Ontong Java, Hawaii, and Samoa
93 suggest that primordial domains are still present in the mantle (Rizo *et al.*, 2016a; Mundl *et*
94 *al.*, 2017).

95 Some of the inefficient mixing evidenced by the longevity of primordial domains could be
96 due to early Earth tectonic regimes differing from those of modern-style plate tectonics
97 (O'Neill and Debaille, 2014). For example, the survival of ^{142}Nd anomaly of $+7\pm3$ ppm in
98 2.72 Ga tholeiites from the Abitibi greenstone belt (AGB), but complete absence of ^{142}Nd
99 anomalies in post-Archean record has been interpreted to indicate a global-scale transition
100 from a stagnant-lid tectonic regime prior to 2.5 Ga to mobile-lid post-Archean plate tectonics
101 (Debaille *et al.*, 2013).

102 Osmium isotope and highly siderophile element (HSE) abundance systematics provide
103 additional information about early Earth processes. For example, the observation that the HSE
104 occur in roughly chondritic relative proportions in the Bulk Silicate Earth (BSE), and that
105 absolute abundances of at least some of the HSE are higher than would be expected from
106 metal-silicate equilibration, have led to the concept of late accretion. Late accretion is
107 commonly envisioned as a process whereby at least 0.5% of Earth's mass was added to the
108 mantle through the continued accretion of planetesimals, subsequent to the cessation of core
109 formation (Chou *et al.*, 1983; Morgan, 1985). Issues related to late accretion are much
110 debated, including the composition of the late accreted materials and the time frame within
111 which they were delivered to Earth and homogenized within the mantle (*e.g.*, (Maier *et al.*,
112 2009; Walker, 2014). Some of the uncertainties stem from the fact that the absolute HSE

113 abundances in the early Earth's mantle are not well constrained, and the causes of their
114 abundance variations are poorly understood. For example, on the basis of measured Pt
115 contents in Archean komatiites, (Maier *et al.*, 2009) argued for a gradual increase in HSE
116 abundances in their presumed deep mantle sources between ~3.5 and ~2.9 Ga, due to slow
117 downward mixing of a “late veneer” of chondritic materials.

118 In this study, we report combined ^{182}Hf - ^{182}W , $^{146,147}\text{Sm}$ - $^{142,143}\text{Nd}$, ^{176}Lu - ^{176}Hf , ^{187}Re - ^{187}Os ,
119 and HSE and lithophile trace element abundance data for 2.72 Ga komatiitic basalts from
120 Boston Creek Township in the AGB. We use the data to (1) constrain the long-term evolution
121 of the mantle domain beneath the Superior Craton that gave rise to the BCF parental magmas,
122 (2) evaluate the degree of late Archean mantle heterogeneity in terms of absolute HSE
123 abundances, based on our previously published and new HSE data, and (3) provide new
124 constraints on the timing of late accretionary processes and mixing times of the Earth's
125 mantle.

126 **2. Geological background, samples, and previous studies**

127 The geology, petrology, and geochemistry of the Boston Creek Flow (BCF) are described
128 in detail by (Stone *et al.*, 1987; Stone *et al.*, 1995a; Stone *et al.*, 1995b) and (Walker and
129 Stone, 2001). The BCF is located in the Ontario portion of the AGB, ~16 km south of
130 Kirkland Lake. Lavas of the AGB are interpreted to have been formed during three volcanic
131 cycles (Cycles I through III: (Jensen and Pyke, 1982). A complete volcanic cycle consisted of
132 a basal komatiite sequence, overlain by a tholeiitic sequence, followed by a calc-alkaline
133 sequence, and capped by an alkaline felsic sequence. The BCF belongs to Cycle II, which is
134 16 km thick and is composed of the komatiitic Wabewawa Group, the tholeiitic Catherine
135 Group, and the calc-alkaline Skead Group; the BCF is located at the top of the Wabewawa
136 Group. A differentiated tholeiitic flow at the base of the Catherine Group, immediately above
137 the BCF, has a U-Pb zircon age of 2720 ± 2 Ma (Corfu and Noble, 1992). This age is

138 interpreted as the age of the entire tholeiitic succession and the BCF, and is similar to the age
139 of komatiites from Munro Township in the northern part of the AGB of 2714 ± 2 Ma (Corfu
140 and Noble, 1992).

141 All Cycle II rocks have been regionally metamorphosed to the prehnite-pumpellyite
142 facies, but portions of the Wabewawa Group, including the BCF, were later contact-
143 metamorphosed to the greenschist facies during intrusion of the Round Lake Batholith (Jolly,
144 1980). The flow can be traced along strike for ~4.6 km, and its thickness varies between 45
145 and 115 m. Samples for this study were collected across the section of the flow exposed near
146 O'Donald Lake, where it is ~100 m thick. In the study area, the flow is subdivided into the
147 upper clinopyroxene spinifex-textured zone and the lower olivine-pyroxene-chromite-
148 titanomagnetite cumulate zone (Fig. 1). The olivine cumulate subzone is ~33 m thick and
149 consists largely of olivine grains 1-3 mm in size completely pseudomorphically replaced by
150 serpentine and magnetite in a matrix of intercumulus pyroxene which itself is partly replaced
151 by tremolite and chlorite. Chromite occurs as euhedral grains up to 1 mm in size either
152 interstitial to or as inclusions in olivine. The upper part of the cumulate zone is occupied by
153 the subzone of olivine-pyroxene cumulate ~7 m thick in the form of equigranular medium-
154 grained rock consisting of pyroxene and olivine grains in a fine-grained matrix of plagioclase,
155 chlorite, actinolite, and opaques. The contact between the cumulate zone and overlying
156 coarse-grained basalt subzone of the spinifex zone is marked by a sharp increase in the
157 proportion of plagioclase. The basalt consists of euhedral grains of clinopyroxene and
158 subhedral grains of plagioclase and titanomagnetite submerged in a groundmass of chlorite,
159 actinolite, plagioclase, epidote and calcite. Further up in the spinifex zone, the coarse-grained
160 basalt subzone is replaced by a subzone of coarse random pyroxene spinifex, then by
161 columnar pyroxene spinifex, and, finally, by fine random pyroxene spinifex at the top of the
162 flow. Most of the spinifex zone above the basalt subzone consists of column-shaped

163 amphibole pseudomorphs after skeletal clinopyroxene grains up to 100 mm long and 0.5-2.0
164 mm wide oriented subperpendicular to the flow boundaries in a matrix of fine-grained
165 plagioclase, chlorite, amphibole, and opaques. At the top and bottom of the spinifex zone, the
166 amphibole pseudomorphs after clinopyroxene are smaller and randomly oriented. In addition,
167 the top of the spinifex-textured zone lacks plagioclase and has a higher proportion of what
168 was once glassy material.

169 The BCF is unique in having an FeO content of the emplaced lava as high as 17 wt. %,
170 strong depletions in Al and heavy rare earth elements (REE), and enrichments in light REE
171 and other highly incompatible lithophile trace elements (Stone *et al.*, 1987; Stone *et al.*,
172 1995a). Rocks from this flow were also shown to be characterized by initial $\varepsilon^{143}\text{Nd}$ of *ca.*
173 +2.5 (Stone *et al.*, 1995a) and $\gamma^{187}\text{Os}$ of -3.8 ± 0.5 (Walker and Stone, 2001).

174 Samples for this study were collected across the BCF (Fig. 1) to attain the largest possible
175 compositional range among individual samples necessary for obtaining a Re-Os isochron and
176 estimating the absolute HSE abundances in its mantle source. The purpose of the new
177 sampling campaign was to collect high-quality material using exclusively metal-free
178 equipment and, with that, to acquire high-precision ^{187}Re - ^{187}Os , ^{176}Lu - ^{176}Hf , $^{146,147}\text{Sm}$ -
179 $^{142,143}\text{Nd}$, ^{182}W isotopic and lithophile trace element, HSE, and W abundance data.

180 **3. Analytical techniques**

181 **3.1. Sample preparation**

182 The samples between 1.0 and 2.0 kg in weight were collected from the surface outcrops
183 using a sledge hammer and cut into rectangular 0.5"×2.0"×3.0" slabs using a diamond saw to
184 remove any sledge hammer marks and signs of alteration. The slabs were then polished on all
185 sides using SiC sandpaper to remove the saw marks, rinsed with milli-Q water, and crushed in
186 an alumina-faced jaw crusher. Small slabs were cut off and used to prepare polished thin
187 sections. A 200-g aliquot of each crushed sample was ground in an alumina shatter box and
188 then finely re-ground in an alumina-faced disk mill. This ground material was used for the
189 chemical studies.

190 **3.2. Major, minor, trace element, and transition metal abundances**

191 Major and minor element analyses were carried out at the Franklin and Marshall College
192 on fused glass discs using a Phillips 2404 XRF vacuum spectrometer and following the
193 protocol of (Mertzman, 2000). Typical accuracy of the analyses was ~2% relative for major
194 elements present in concentrations greater than 0.5% and ~5% relative for the rest of the
195 major and the minor elements as determined via analysis of the USGS GRM BIR-1, BCR-1,
196 and BHVO-2 as unknowns (Table 1).

197 The abundances of the trace elements were determined using the standard addition
198 solution inductively-coupled plasma mass-spectrometry technique (SA ICP-MS) following
199 the protocol outlined in (Puchtel *et al.*, 2016b). Between 25 and 35 mg of sample powder
200 were weighed out in 15 mL screw-cap Savillex Teflon vials. Approximately 0.5 mL double-
201 distilled concentrated HNO₃ and 3 mL double-distilled concentrated HF were added, the vials
202 were sealed and kept on a hotplate at 200°C for 48 hours. The vials were then opened, the
203 sample solutions evaporated to dryness, 0.5 mL of distilled SeaStar concentrated HClO₄
204 added to the dry residue to convert fluorides into perchlorates, the vials sealed again and kept
205 on a hotplate at 200°C for 48 hours. The vials were re-opened and the sample solutions dried
206 down on the hotplate at 230°C. This step was followed by re-dissolution of the residue in 2
207 mL of 6M HCl to convert it into the chloride form. This step was repeated. The dry residue
208 was taken up in ~10 grams of 0.8M HNO₃ (with the exact weight recorded), and this stock
209 solution was used for preparing spiked aliquots used for ICP-MS measurements. Two
210 standard addition spikes were prepared, one containing concentrated mixed solutions of Y and
211 Zr, and the other containing Nb, Hf, Th, U, and REE. Three aliquots of each sample, each
212 containing ~1.0 gram of sample stock solution (with the exact weight recorded), were
213 prepared for each of the two groups of the elements to be analyzed, one containing no spike,
214 one with the amount of spike containing 2× the estimated amount of element present in the
215 sample aliquot, and one with the amount of spike containing 4× the estimated amount of
216 element present in the sample aliquot, with the exact weights of the spikes recorded. One total
217 analytical blank (TAB) was also prepared and measured with every batch of six samples.
218 Approximately 100 mg (with the exact weight recorded) of 500 ppb In solution was added to
219 each sample aliquot and the TAB solutions to monitor and correct for signal drift during
220 analysis, and the one sample- and two sample-spike solutions for each sample were diluted to
221 10 grams with 0.8M HNO₃.

222 The sample solutions were analyzed on a *ThermoFisher Element2* sector field ICP-MS at
223 the *Plasma Laboratory (PL)*, University of Maryland. Prior to analysis, the instrument was

224 thoroughly tuned to maximize sensitivity and minimize oxide production, and mass-
225 calibrated. The intensities of selected isotopes of each element were measured in either low
226 resolution (lithophile trace elements) or medium resolution (transition metals) modes. The
227 raw data were reduced using an in-house Excel macro. The in-run uncertainties on the
228 concentrations were typically better than 1% for all elements (2SE). The accuracy and
229 precision of the analyses were determined via replicate analysis of the USGS GRM BIR-1 and
230 BCR-1 (Puchtel *et al.*, 2016b); for most elements, it was ~5% (2SD), which includes the
231 uncertainty introduced by the SRM powder heterogeneity.

232 **3.3. Re-Os isotopic compositions and HSE abundances**

233 To obtain the Re-Os isotopic and HSE abundance data, ca. 1.5 g whole-rock powder, 6
234 mL purged, triple-distilled concentrated HNO₃, 4 mL triple-distilled concentrated HCl, and
235 appropriate amounts of mixed ¹⁸⁵Re-¹⁹⁰Os and HSE (⁹⁹Ru, ¹⁰⁵Pd, ¹⁹¹Ir, ¹⁹⁴Pt) spikes were sealed
236 in double internally-cleaned, chilled 25 mL Pyrex™ borosilicate Carius Tubes (CTs) and
237 heated to 270°C for 96 h. Osmium was extracted from the acid solution by CCl₄ solvent
238 extraction (Cohen and Waters, 1996), back-extracted into HBr, and purified via
239 microdistillation (Birck *et al.*, 1997). Ruthenium, Pd, Re, Ir, and Pt were separated and
240 purified using anion-exchange chromatography following a modified protocol of (Rehkämper
241 and Halliday, 1997).

242 Osmium isotopic measurements were done *via* negative thermal ionization mass
243 spectrometry (N-TIMS: (Creaser *et al.*, 1991). All samples were analyzed using a secondary
244 electron multiplier (SEM) detector of a *ThermoFisher Triton* mass spectrometer at the *Isotope*
245 *Geochemistry Laboratory (IGL)*, University of Maryland. The measured isotopic ratios were
246 corrected for mass fractionation using ¹⁹²Os/¹⁸⁸Os = 3.083. The internal precision of measured
247 ¹⁸⁷Os/¹⁸⁸Os for all samples was between 0.03% and 0.05% relative. The ¹⁸⁷Os/¹⁸⁸Os ratio of
248 300-500 pg loads of the in-house *Johnson-Matthey* Os standard measured during the two-year
249 period leading up to the current analytical sessions averaged 0.11376±10 (2SD, N = 64). This
250 value characterizes the external precision of the isotopic analyses (0.10%), which was used to
251 estimate the true uncertainty on the measured ¹⁸⁷Os/¹⁸⁸Os ratio for each individual sample.
252 The measured ¹⁸⁷Os/¹⁸⁸Os ratios were further corrected for instrumental mass bias relative to
253 the average ¹⁸⁷Os/¹⁸⁸Os = 0.11379 measured for the *Johnson-Matthey* Os standard on the
254 Faraday cups of the *IGL Triton* (Puchtel *et al.*, 2016b). The correction factor of 1.00026 was
255 calculated by dividing this value by the average ¹⁸⁷Os/¹⁸⁸Os measured for the *Johnson-*
256 *Matthey* Os standard on the SEM of the same instrument.

257 The measurements of Ru, Pd, Re, Ir, and Pt were performed at the *PL* via ICP-MS using a
258 *Nu Plasma* instrument with a triple electron multiplier configuration in static mode. Isotopic
259 mass fractionation was monitored and corrected for by interspersing samples and standards.
260 The accuracy of the data was assessed by comparing the results for the reference materials
261 UB-N and GP-13 with results from other laboratories (Puchtel et al., 2014). In this study, we
262 also analyzed several additional reference materials, including IAG MUH-1 (Austrian
263 harzburgite), IAG OKUM (Ultramafic rock) and NRC TDB-1 (Diabase PGE Rock Material);
264 these data are reported in Table 2, together with the reference values. MUH-1 and OKUM
265 have compositions similar to the BCF cumulate samples with high Os, Ir, and Ru abundances,
266 whereas TDB-1 is similar to the spinifex-textured samples with low Os, Ir, and Ru
267 abundances. Concentrations of all HSE and Os isotopic compositions obtained at the *IGL* are
268 in good agreement with the certified reference values. Diluted spiked aliquots of iron
269 meteorites were run during each analytical session as secondary standards. The results from
270 these runs agreed within 0.5% for Re and Ir, and within 2% for Ru, Pt, and Pd, with
271 fractionation-corrected values obtained from measurements of undiluted iron meteorites using
272 Faraday cups on the same instrument with a signal of >100 mV for the minor isotopes. Blank
273 contributions were less than these values for the respective elements. The average TAB
274 during the analytical campaign was (in pg): Ru 4.2, Pd 5.3, Re 0.28, Os 0.43, Ir 0.47, and Pt
275 95 ($N = 3$). The average TAB constituted less than 0.1% for Os for the majority of samples
276 except for those with low Os abundances, for which it varied between 0.2 and 0.7%, less than
277 0.5% for Re, Ir, Ru, and Pd, and less than 2% for Pt of the total element analyzed in the
278 samples. We therefore cite ± 0.1 to $\pm 0.7\%$ as the uncertainty on the concentrations of Os, $\pm 2\%$
279 as the uncertainty on the concentrations of Ru, Pt, and Pd, and $\pm 0.5\%$ as the uncertainty on
280 the concentrations of Re and Ir. The uncertainty on the Re/Os ratio was calculated for each
281 particular sample via multiplying the uncertainties on the Re and Os abundances for this
282 sample. These uncertainties vary between 0.6 and 1.1% relative.

283 The regression calculations were performed using ISOPLOT 3.00 (Ludwig, 2003). The
284 uncertainties on the concentrations and isotopic ratios used for the regression calculations are
285 those stated above. The initial $\gamma^{187}\text{Os}$ values were calculated as the per cent deviation of the
286 isotopic composition at the time defined by the Re-Os isochron relative to the chondritic
287 reference of (Shirey and Walker, 1998) at that time.

288 The average chondritic Os isotopic composition at the time defined by the isochron was
289 calculated using the ^{187}Re decay constant $\lambda = 1.666 \times 10^{-11} \text{ year}^{-1}$, an early Solar System initial

290 $^{187}\text{Os}/^{188}\text{Os} = 0.09531$ at $T = 4558$ Ma, and $^{187}\text{Re}/^{188}\text{Os} = 0.40186$ (Smoliar *et al.*, 1996;
291 Shirey and Walker, 1998).

292 **3.4. Tungsten isotopic compositions and abundances**

293 The W isotope and concentration measurements were carried out at the *IGL* following the
294 chemical procedures described in (Touboul *et al.*, 2014) for purifying W, and measurement
295 techniques developed by (Touboul and Walker, 2012) for determining W isotope
296 compositions. For each isotopic analysis, between 2 and 5 grams of sample powder was
297 processed to obtain the $\sim 1 \mu\text{g}$ of W necessary for high-precision W isotope measurements.
298 The sample powders were digested in 60 mL Savillex Teflon screw-cap vials using a 5:1
299 mixture of double-distilled concentrated HF and HNO₃ on a hot plate at 150°C for one week
300 and dried down. The residues were digested in a mixture of 20 mL concentrated HNO₃ and
301 0.1 mL H₂O₂ at 120°C for 24 hours and dried down. This step was repeated. The residues
302 were converted into the chloride form by repeated dissolutions in double-distilled 6M HCl
303 and subsequent dry downs. The residues were finally re-dissolved in 10 mL of a mixture of
304 1M HCl and 0.1M HF. The sample solutions were centrifuged and the W in the supernatant
305 was separated and purified using the four-stage ion-exchange chromatography protocol
306 described in (Touboul and Walker, 2012), with minor modifications. The third stage
307 involving a 1.5 mL anion-exchange column was repeated to improve the separation of Ti
308 from W, which significantly increased W ionization efficiency. Tungsten recovery using this
309 procedure was better than 90% for all samples analyzed.

310 Tungsten isotopic compositions were measured by N-TIMS on the *ThermoFisher Triton*
311 mass-spectrometer at the *IGL* using a 2-line multi-static acquisition protocol and following
312 the technique described by (Touboul and Walker, 2012). This technique relies on a double-
313 normalization procedure for correcting the W isotope fractionation (using the $^{186}\text{W}/^{183}\text{W}$ ratio
314 and an exponential law) and O isotope fractionation (using the $^{183}\text{W}/^{184}\text{W}$ ratio and a linear
315 law). In contrast to a more recent analytical technique developed by (Archer *et al.*, 2017),
316 where the O isotopic composition is determined during the analysis, our technique does not
317 provide independent $^{183}\text{W}/^{184}\text{W}$ data. The long-term external precision (2SD) of the analysis
318 was ± 4.5 ppm on the $^{182}\text{W}/^{184}\text{W}$ ratio based on multiple measurements of the *Alfa Aesar* W
319 standard solution. At the end of the useful life of the Faraday cups of the *Triton*, the external
320 reproducibility tended to slightly increase, as the $^{182}\text{W}/^{184}\text{W}$ ratios started to drift. During the
321 entire duration of the present analytical campaign (from 02/2013 through 11/2014), this
322 decrease in the external reproducibility was observed in 03/2014 and 06/2014, after which the

323 Faraday cups were immediately replaced. For the samples measured in 03/2014 and 06/2014,
324 the $\mu^{182}\text{W}$ values were calculated relative to the average $^{182}\text{W}/^{184}\text{W}$ ratios of the *Alfa Aesar* W
325 standard measured in 03/2014 (magazines 324 and 325) and 06/2014 (magazines 326 and
326 327). For the rest of the samples, the $\mu^{182}\text{W}$ values were calculated relative to the long-term
327 average $^{182}\text{W}/^{184}\text{W}$ ratios measured in the *Alfa Aesar* W standard between 02/2013 and
328 11/2014 (magazines 264 to 313 and 340 to 342).

329 Total procedural blanks averaged ~1.8 ng, which was less than 0.2% of the total W
330 present in the analyzed W cuts. Blank corrections on the measured W isotope composition,
331 therefore, were negligible.

332 Tungsten abundances were determined by isotope dilution ICP-MS. Between 100 and 200
333 mg of sample powder and a ^{182}W -enriched spike were equilibrated in 15 mL screw-cap
334 *Savillex* Teflon vials using a 5:1 mixture of double-distilled concentrated HNO_3 and HF at
335 180°C for 3-4 days, followed by the dry down of the solutions. Residues were treated with
336 double-distilled concentrated HNO_3 and traces of H_2O_2 at 120°C for 24 hours. After
337 evaporation to dryness, residues were converted into the chloride form by adding 6M HCl,
338 followed by another dry down. Residues were then equilibrated with a 6M HCl-0.01M HF
339 mixture at 120°C for ~24 h, after which complete dissolution usually was achieved. Finally,
340 solutions were dried down and residues re-dissolved in 2 mL of a 0.5M HCl + 0.5M HF
341 mixture, and W purified using a previously established anion-exchange chromatography
342 technique (*e.g.*, (Kleine *et al.*, 2004a).

343 The W isotopic compositions of the spiked samples were measured using the *Nu Plasma*
344 ICP-MS at the *PL*. The total analytical blank for W averaged 170 ± 50 pg, corresponding to
345 contributions of <1% of the total W present in the samples.

346 **3.5. Sm-Nd isotopic compositions and abundances**

347 The Sm-Nd isotopic studies were carried out at the *IGL* following the techniques outlined
348 in (Puchtel *et al.*, 2016a). Between 200 and 300 mg of sample powder for each sample were
349 tightly sealed with Teflon tape in a screw-cap 15 mL *Savillex* Teflon vial with 5 mL double-
350 distilled concentrated HF and 1 mL double-distilled concentrated HNO_3 and digested on a
351 hotplate at 200°C for 24 hours. The vessels were opened, the solutions dried down, new
352 batches of acids added, and the digestion step was repeated at 200°C for 48 hours. After the
353 solutions were again dried down, 0.5 mL of concentrated *SeaStar* HClO_4 were added, the
354 vials sealed and kept on a hotplate at 200°C for 24 hours. The solutions were then dried down
355 at ~230°C, and the residues converted into the chloride form using 6M HCl. This step was

356 repeated twice. The residue was then taken up in 5 g of 2.5M HCl (with the exact weight
357 recorded) and a ~3% aliquot of the sample solution was weighed out (with the exact weight
358 recorded) and used for determination of the $^{147}\text{Sm}/^{144}\text{Nd}$ ratios via the SA ICP-MS technique
359 (without a knowledge of the precise weight of the sample represented by the amount of the
360 sample aliquot, only the Sm/Nd ratios were determined). From the remaining sample solution,
361 REE were first separated from the silicate matrix using standard cation-exchange
362 chromatography. The Nd fractions were further separated from the other REEs using first 2-
363 methylsuccinic acid cation-exchange chromatography and then HDEHP chromatography. The
364 resultant Nd cuts were used for high-precision measurements of the Nd isotopic compositions.

365 Measurements of the Nd isotopic compositions were performed on the *ThermoFisher*
366 *Triton* mass-spectrometer at the *IGL*, using a two-line acquisition protocol and a multi-
367 dynamic routine. For each sample load, between 2400 and 3600 ratios were collected with 8
368 sec. integration times in blocks of 20 ratios each. For every three blocks of data collection, the
369 two peaks were centered, the ion beam was re-focused, and the amplifiers were electronically
370 rotated relative to the Faraday cup detectors. A 30 sec. baseline measurement per block was
371 performed for each Faraday cup/amplifier pair by beam deflection. The effects of
372 instrumental mass fractionation were corrected relative to $^{146}\text{Nd}/^{144}\text{Nd} = 0.7219$ using an
373 exponential law. A total of 10 loads of 900 ng of the Nd standard AMES were run at the
374 beginning and end of the analytical session, with 2400 ratios collected during each
375 measurement. During the measurements, the signal intensities for both the standards and the
376 samples were kept at constant levels, between 3V and 5V on the ^{142}Nd mass. The calculated
377 $^{147}\text{Sm}/^{144}\text{Nd}$ ratios were between 10^{-5} and 10^{-6} , meaning that corrections for Sm isobaric
378 interferences were negligible. The calculated $^{142}\text{Ce}/^{142}\text{Nd}$ ratios were between 10^{-5} and 10^{-4} ,
379 resulting in interference corrections of >10 ppm on the $^{142}\text{Nd}/^{144}\text{Nd}$ ratio in some samples. No
380 correlation between measured $^{142}\text{Nd}/^{144}\text{Nd}$ and the intensity of the ^{140}Ce signal was observed,
381 indicating that these interferences were adequately corrected for. During the course of the
382 present analytical campaign, the external reproducibility of the AMES Nd standard solution
383 measurements was ± 2.8 ppm for $^{142}\text{Nd}/^{144}\text{Nd}$ and ± 3.5 ppm for $^{143}\text{Nd}/^{144}\text{Nd}$ (2SD, $N = 34$).
384 The $^{142}\text{Nd}/^{144}\text{Nd}$ ratios are expressed in $\mu^{142}\text{Nd}$ units calculated as part per million (ppm)
385 deviations from the average $^{142}\text{Nd}/^{144}\text{Nd}$ ratio of the AMES Nd standard obtained during the
386 course of the analytical campaign.

387 The $^{147}\text{Sm}/^{144}\text{Nd}$ ratios used for calculating the initial $^{143}\text{Nd}/^{144}\text{Nd}$ isotopic ratios obtained
388 during the high-precision runs were determined using the SA ICP-MS technique. The
389 precision and accuracy of determining the $^{147}\text{Sm}/^{144}\text{Nd}$ ratio was assessed by analyzing

multiple aliquots of the USGS GRM BCR-1 and BIR-1. The average values obtained during the course of this analytical campaign were 0.1397 ± 8 ($N = 4$, 2SD) and 0.2798 ± 24 ($N = 18$, 2SD) for BCR-1 and BIR-1, respectively (Puchtel *et al.*, 2016b). The average $^{147}\text{Sm}/^{144}\text{Nd}$ ratio for BCR-1 is identical, within the uncertainty, to the average $^{147}\text{Sm}/^{144}\text{Nd} = 0.13939 \pm 16$ ($N = 4$, 2SD) obtained at the *IGL* using the ID-TIMS technique (Puchtel *et al.*, 2013). The larger uncertainty on the $^{147}\text{Sm}/^{144}\text{Nd}$ ratio obtained for BIR-1 in this study (0.9%) compared to BCR-1 (0.5% relative) can be ascribed either to the apparently slightly larger sample powder heterogeneity of BIR-1 compared to BCR-1 (Puchtel *et al.*, 2016a) or lower REE abundances in BIR-1 compared to BCR-1. Since the REE concentration range in the BCF is more similar to REE abundances in BCR-1, we used the external reproducibility of the $^{147}\text{Sm}/^{144}\text{Nd}$ ratio obtained for BCR-1 as a measure of uncertainty on the $^{147}\text{Sm}/^{144}\text{Nd}$ obtained in this study (0.5%, 2SD).

The initial $\varepsilon^{143}\text{Nd}$ values were calculated based on the present-day parameters of the Chondritic Uniform Reservoir (CHUR): $^{147}\text{Sm}/^{144}\text{Nd} = 0.1967$ (Jacobsen and Wasserburg, 1980), $^{143}\text{Nd}/^{144}\text{Nd} = 0.512638$ (Hamilton *et al.*, 1983).

3.6. Lu-Hf isotopic compositions and abundances

The Lu-Hf concentration and isotopic measurements were carried out at the Ecole Normale Supérieure de Lyon (ENSL), France. The sample dissolution procedure, employing Parr bombs and a mixed >98% pure ^{176}Lu - ^{180}Hf spike, and the Lu and Hf separation protocols used are described in (Blichert-Toft *et al.*, 1997), (Blichert-Toft, 2001), and (Blichert-Toft and Puchtel, 2010). Lutetium and Hf isotopic compositions were measured by multi-collector ICP-MS using the *Nu Plasma 500 HR* coupled with a *DSN-100* desolvating nebulizer and following the protocols of (Blichert-Toft *et al.*, 1997; Blichert-Toft *et al.*, 2002). Hafnium was normalized for instrumental mass fractionation relative to $^{179}\text{Hf}/^{177}\text{Hf} = 0.7325$ using an exponential law. The JMC-475 Hf standard was analyzed every two samples and gave, during the present single analytical session, an average $^{176}\text{Hf}/^{177}\text{Hf} = 0.282164 \pm 0.000010$ (2SD; $N = 8$), which represents the estimate of the external precision of the Hf isotopic analyses (0.0035%). Since this value is identical, within uncertainty, to the accepted value for the JMC-475 Hf standard of 0.282163 ± 0.000009 (Blichert-Toft and Albarède, 1997), no further corrections were applied to the data. We used the uncertainty obtained from the external reproducibility of the Hf standard as the uncertainty on the Hf isotopic composition for the isochron calculations, except for the two samples (BC08 and BC10; Table S7) for which the internal run precision was slightly larger than the external reproducibility, in which case the

423 in-run error was used. The uncertainty on the Lu/Hf ratio was 0.2% and this was the value we
424 used for the isochron calculations for all samples. Total analytical blanks were <20 pg for
425 both Lu and Hf.

426 For the isochron calculations, ISOPLOT 3.00 (Ludwig, 2003) and the ^{176}Lu decay
427 constant of $1.867 \times 10^{-11} \text{ year}^{-1}$ (Scherer et al., 2001; Söderlund et al., 2004) were used. The
428 $\varepsilon^{176}\text{Hf}$ values were calculated as parts per 10,000 deviation of the measured sample
429 $^{176}\text{Hf}/^{177}\text{Hf}$ at the time of komatiite lava emplacement from the chondritic reference defined as
430 $^{176}\text{Lu}/^{177}\text{Hf} = 0.0336$ and $^{176}\text{Hf}/^{177}\text{Hf} = 0.282785$ (Bouvier et al., 2008).

431 **4. Results**

432 ***4.1. Major and lithophile trace element abundances***

433 Major and trace element concentration data for the BCF are listed in Tables 3 and 4, and
434 selected elements are plotted on variation diagrams in Fig. 2 and as BSE-normalized values in
435 Fig. 3. The elemental abundances vary in the regular fashion typical of thick differentiated
436 komatiitic basalt lava flows, such as the Fred's Flow in the AGB (Arndt, 1977). The MgO
437 abundances range between 13.4 and 8.17 wt. % in the clinopyroxene-spinifex zone, increase
438 to 28.5 wt. % in the uppermost part of the cumulate zone and reach a maximum of 34.0 wt. %
439 about halfway down the cumulate zone. The rocks are characterized by high total Fe_2O_3
440 abundances of up to 19.3 wt. % in the spinifex zone and 22.2 wt. % in the cumulate zone
441 (Table 3).

442 Most lithophile trace element abundances plot on well-defined trends with negative slopes
443 in MgO versus trace element variation diagrams (Fig. 2). As is evident from Fig. 2, the BCF
444 is significantly depleted in Al_2O_3 ($\text{Al}_2\text{O}_3/\text{TiO}_2 = 5.2 \pm 0.2$, 2SE) relative to the typical Al-
445 undepleted komatiites from Munro Township. These correlations reflect mainly olivine, with
446 subordinate clinopyroxene, control over the BCF compositional range. These trends further
447 indicate immobile behavior of most elements of interest during secondary alteration
448 processes.

449 The BSE-normalized lithophile trace element abundances are characterized by
450 enrichments in light REE ((La/Sm)_N = 1.88±0.05, 2SE) and depletions in heavy REE
451 ((Gd/Yb)_N = 2.02±0.05, 2SE); all samples exhibit small negative Zr and Hf anomalies (Fig.
452 3). Based on the coupled depletions in Al₂O₃ and heavy REE, the BCF lava belongs to the Al-
453 depleted komatiite type of (Nesbitt *et al.*, 1979).

454 **4.2. Re-Os isotopic compositions and HSE abundances**

455 The Re-Os isotopic and HSE abundance data for the BCF are listed in Table 5 and plotted
456 on a Re-Os isochron diagram in Fig. 4, on the CI chondrite-normalized spider diagram in Fig.
457 5, and on MgO versus HSE variation diagrams in Fig. 6. Thirteen samples (including
458 replicates and excluding sample BC06, which plots well above the regression line), define a
459 regression line with a slope corresponding to an ISOPLOT Model 3 age of 2728±23 Ma and a
460 chondritic, albeit imprecise, initial $^{187}\text{Os}/^{188}\text{Os} = 0.1122\pm38$ ($\gamma^{187}\text{Os} = +3.6\pm3.4$). This age is
461 in agreement with the U-Pb zircon age of 2720±2 Ma obtained by (Corfu and Noble, 1992)
462 for the tholeiitic succession that hosts the BCF. The large uncertainty on the initial $\gamma^{187}\text{Os}$
463 value derived from the regression is due to scatter (MSWD = 140) of the data for samples
464 with high $^{187}\text{Re}/^{188}\text{Os}$ ratios. Averaging the initial $^{187}\text{Os}/^{188}\text{Os}$ ratios for samples with
465 $^{187}\text{Re}/^{188}\text{Os} < 0.5$, which also have the highest Os abundances, yields a more precise average
466 initial $\gamma^{187}\text{Os(T)} = -0.58\pm0.90$ (2SD). This chondritic value is inconsistent with the
467 subchondritic $\gamma^{187}\text{Os}$ value of -3.8 ± 0.5 obtained by (Walker and Stone, 2001), even though
468 the Re-Os ages obtained in the two studies are identical within their respective uncertainties
469 (2708±13 and 2728±23 Ma).

470 The source of this discrepancy is not clear. Data for sample powders J17 and 2-18
471 analyzed in both studies show ~50% higher Re abundances in the study by (Walker and
472 Stone, 2001); this resulted in 1.5-3.1% lower calculated initial $\gamma^{187}\text{Os}$ values for these samples
473 compared to the present study (Table 5). One potential explanation is under-correction of the

474 total analytical blank for Re (17 ± 5 pg compared to 0.34 pg in this study) given the very low
475 Re abundances in the cumulate samples. Additionally, from the *un-crushed material* of the
476 Walker and Stone (2001) study we prepared a new powder for sample J17 (labeled J17_1)
477 using metal-free equipment. This new sample powder has 46% lower Re abundance
478 compared to the powder for this sample from the Walker and Stone (2001) study that we also
479 analyzed here (Table 5). This may be due to minor Re contamination during sample
480 preparation in the Walker and Stone (2001) study because of the very low Re abundances in
481 these samples (0.048 ppb Re in the new sample powder J17_1). Correction of the 46% surplus
482 Re brings the calculated initial $\gamma^{187}\text{Os}$ value for sample powder J17 up to an average of +0.11
483 (based on our two replicate analyses), which is similar to the average initial $\gamma^{187}\text{Os}$ value of
484 +0.50 obtained on two replicate analyses of the new powder for this sample, J17_1.

485 Due to the lack of un-crushed material for sample 2-18, we were unable to evaluate the
486 degree of Re contamination (if any) of this sample; as a result, we used uncorrected $\gamma^{187}\text{Os}$
487 values for this sample in calculating the average initial $\gamma^{187}\text{Os}$. When re-calculating the
488 average initial $\gamma^{187}\text{Os}$ for the low- $^{187}\text{Re}/^{188}\text{Os}$ samples and including the contamination-
489 corrected $\gamma^{187}\text{Os}$ for sample J17, a precise average initial $\gamma^{187}\text{Os} = +0.06\pm0.34$ is obtained.
490 This value is our best estimate of the initial $^{187}\text{Os}/^{188}\text{Os}$ isotopic composition of the BCF
491 mantle source.

492 In the CI chondrite-normalized diagrams (Fig. 5) and MgO versus HSE variation
493 diagrams (Fig. 6), Os, Ir, and Ru abundances increase in the samples from the cumulate zone
494 compared to those from the spinifex zone; however, Os and Ir, and to a lesser extent Ru,
495 abundances also show large (*e.g.*, Os = 0.16–3.0 ppb) variations within the samples from the
496 cumulate zone itself, which are independent of the MgO content in these samples. This type
497 of variation is typical of the so-called Munro-type lavas (Puchtel and Humayun, 2005), where

498 abundances of these elements are controlled mostly by fractionation of Os-Ir alloy during lava
499 differentiation upon emplacement.

500 Platinum and Pd abundances exhibit strong negative correlations with MgO contents and
501 decrease from spinifex to cumulate zone of the BCF (Fig. 5); the data plot on the trends that
502 intersect the MgO axes at 53 ± 2 and 48 ± 1 wt. % MgO, respectively (Fig. 6). While the trend
503 for Pd is consistent with olivine control, the trend for Pt is somewhat shallower, indicating
504 presence on the liquidus of a phase in addition to olivine that affected to some extent
505 variations of Pt during differentiation of the BCF.

506 Finally, Re abundances in the spinifex-textured samples plot with significant scatter (Fig.
507 6). This likely indicates Re mobility during alteration of the BCF, including gain/loss of Re in
508 the spinifex-textured samples and net loss in the cumulate samples. The observed Re mobility
509 evidently took place shortly after emplacement of the BCF, with the Re-Os system remaining
510 undisturbed since then, as evidenced by the correct Re-Os isochron age obtained.

511 **4.3. *W* isotopic compositions and abundances**

512 Tungsten abundances and isotopic compositions are listed in Table 6 and plotted in Figs.
513 2-3 and 7. The W abundances vary from 245 to 1305 ppb. The highest W abundance (1305
514 ppb) is observed in sample powder J17 from the Walker and Stone (2001) study. In the new
515 sample powder J17_1 that was prepared for this study from un-crushed material of sample J17
516 using metal-free equipment, the W concentration is $\sim 4\times$ lower (347 ppb). This is consistent
517 with the $\sim 50\%$ higher Re abundance in sample J17 compared to J17_1 and supports the
518 conclusion that sample J17 was contaminated with metal during sample preparation in the
519 Walker and Stone (2001) study. Sample 2-18, which has a $\sim 2\times$ higher W abundance
520 compared to sample J17_1, was also likely contaminated with W (and possibly Re) during
521 sample preparation in the Walker and Stone (2001) study, although to a lesser degree than

522 sample J17. As such, W abundance data for samples J17 and 2-18 were excluded from further
523 discussion and no W isotopic data were obtained for these samples for the same reason.

524 In the MgO versus trace element diagrams (Fig. 2), W abundances plot with significant
525 scatter around a trend with a slightly positive slope. The BSE-normalized trace element
526 abundances (Fig. 3) are characterized by variable positive W anomalies relative to
527 neighbouring elements (*i.e.*, Th and U) with similar incompatibility during mantle melting
528 ($W/W^* = 1.6\text{--}13$, where $W/W^* = W_N/(\sqrt{[Th_N \times U_N]})$, and N are BSE normalized values from
529 (Arevalo and McDonough, 2008) and (Hofmann, 1988). In the upper part of the spinifex
530 zone, the W/W^* ratio varies between 1.6 and 2.4, indicating presence of only a small positive
531 W abundance anomaly. Across the BCF, W abundances increase in the cumulate zone relative
532 to the spinifex zone, displaying a positive correlation with MgO contents (Fig. 2). There is
533 also a positive correlation between W/W^* and LOI values (Fig. 3b).

534 All the BCF samples analyzed are characterized by $^{182}\text{W}/^{184}\text{W}$ ratios higher than the
535 $^{182}\text{W}/^{184}\text{W}$ measured in the terrestrial standard, with an average $\mu^{182}\text{W}$ value of $+11.7\pm4.5$
536 (2SD, $n = 12$), where $\mu^{182}\text{W}$ is the parts per million deviation of $^{182}\text{W}/^{184}\text{W}$ of a given sample
537 from that of the terrestrial standard, which, by definition, is equal to zero (Table 6, Fig. 7).

538 **4.4. Sm-Nd and Lu-Hf isotopic compositions and abundances**

539 The Sm-Nd isotopic data for the BCF are listed in Table 7 and plotted in Figs. 8 and 9. All
540 samples analyzed are characterized by small ^{142}Nd deficits, with an average $\mu^{142}\text{Nd} =$
541 -3.8 ± 2.8 (2SD, $n = 15$), where $\mu^{142}\text{Nd}$ is the parts per million deviation of $^{142}\text{Nd}/^{144}\text{Nd}$ of a
542 given sample from that of the terrestrial standard, which, by definition, is equal to zero (Table
543 7, Fig. 8). The average $^{142}\text{Nd}/^{144}\text{Nd}$ of the BCF, however, is not resolvable, within the
544 uncertainty, from that of the terrestrial Nd standard AMES analyzed during the course of this
545 analytical campaign ($\mu^{142}\text{Nd} = 0.0\pm2.8$, 2SD; $N = 34$).

546 The ^{147}Sm - ^{143}Nd data (Fig. 9a) for the BCF yield a Model 1 ISOPLOT isochron age of
547 2719 ± 170 Ma (MSWD = 0.89), which is identical to the U-Pb emplacement age of 2720 ± 2
548 Ma. This indicates that the samples from the BCF behaved as closed systems with regard to
549 their Sm–Nd isotope systematics. This conclusion is also supported by the magmatic nature of
550 the variations of the Sm and Nd abundances in the samples across the BCF as a function of
551 their MgO contents (Fig. 2). Due to the limited variation in the Sm/Nd ratio among the
552 samples, the ISOPLOT regression analysis produced a rather imprecise isochron age and an
553 initial $\varepsilon^{143}\text{Nd} = +2.6\pm3.0$, where $\varepsilon^{143}\text{Nd}$ is the parts per ten thousand deviation of the
554 $^{143}\text{Nd}/^{144}\text{Nd}$ ratio of a given sample from the chondritic, or BSE, reference value. A more
555 precise initial $\varepsilon^{143}\text{Nd} = +2.5\pm0.2$ (2SD, $n = 15$) is obtained by averaging the initial
556 $^{143}\text{Nd}/^{144}\text{Nd}$ ratios calculated for each sample using the measured $^{147}\text{Sm}/^{144}\text{Nd}$ and
557 $^{143}\text{Nd}/^{144}\text{Nd}$ ratios and the BCF emplacement age of 2720 Ma.

558 The ^{176}Lu - ^{176}Hf data (Fig. 9b) for the BCF define a correlation in $^{176}\text{Lu}/^{177}\text{Hf}$ – $^{176}\text{Hf}/^{177}\text{Hf}$
559 space corresponding to a Model 3 ISOPLOT age of 2489 ± 880 Ma (MSWD = 5.4), which also
560 overlaps, within the uncertainties, the U-Pb emplacement age of the BCF. As with the Sm-Nd
561 isotopic system, the limited range in the Lu/Hf ratios among the samples precludes
562 determination of more precise age and initial $\varepsilon^{176}\text{Hf}$, defined as the parts per ten thousand
563 deviation of the $^{176}\text{Hf}/^{177}\text{Hf}$ ratio of a given sample from the chondritic reference value (Table
564 8, Fig. 9b). Averaging initial $\varepsilon^{176}\text{Hf}$ values of individual samples calculated using the
565 measured $^{176}\text{Lu}/^{177}\text{Hf}$ and $^{176}\text{Hf}/^{177}\text{Hf}$ ratios and the BCF emplacement age of 2720 Ma yields
566 a more precise average initial $\varepsilon^{176}\text{Hf} = +4.2\pm0.9$ (2SD, $n = 6$).

567 Similar to other late Archean and post-Archean komatiite and basalt systems, the
568 calculated initial $\varepsilon^{143}\text{Nd}$ and $\varepsilon^{176}\text{Hf}$ ratios of the BCF plot on the terrestrial array of (Blichert-
569 Toft and Puchtel, 2010), indicating coupled, or congruent, normal depleted mantle behavior of
570 the Nd-Hf isotope systems in the mantle source of the BCF (Fig. 9c).

571 **5. Discussion**

572 **5.1. Komatiite or picrite?**

573 There is some controversy in the literature regarding the composition of the parental
574 magma (komatiitic or picritic) and the source of the BCF. In their original study, (Stone *et al.*,
575 1987) emphasized that the BCF exhibited the two most important features of komatiitic rocks:
576 spinifex-texture and the crystallization sequence Ol – Cpx – Pl. Based on the geochemical
577 similarity of the BCF to the Al-depleted komatiites from the Barberton GB and the textural
578 and petrographic features typical of komatiites, these authors concluded that the BCF was an
579 example of a thick, layered, Al-depleted komatiite that may have been derived from an Fe-
580 and Ti-enriched lower mantle following development of a chemically layered mantle during
581 the Archean. (Walker and Stone, 2001) referred to the BCF as an Fe-enriched komatiite flow.
582 These authors concluded that the parental melt to the BCF was either derived from early
583 Archean, melt-depleted subcontinental lithospheric mantle (based on the strongly
584 subchondritic initial $^{187}\text{Os}/^{188}\text{Os}$ isotopic composition that has not been confirmed in this
585 study), or was sourced from a portion of the mantle that retained some characteristics of early
586 Earth formation, such as majorite fractionation from a primordial magma ocean.

587 In the recent compilation by (Arndt *et al.*, 2008), the BCF was referred to as komatiite and
588 was argued to be similar to the other Fe- and Ti-enriched, Al-depleted komatiites, *e.g.*, from
589 the 3.0 Ga Meekatharra–Wydgee GB of the Yilgarn Block in Western Australia (Barley *et al.*,
590 2000), the 2.93 Ga Steep Rock and Lumby Lake GB in the Northern Superior Province,
591 Canada (Hollings and Wyman, 1999; Tomlinson *et al.*, 1999), the 2.70 Ga Vermillion GB of
592 Minnesota (Green and Shulz, 1977; Schulz, 1982), the 2.11 Ga Inini GB of the Guiana shield
593 (Capdevila *et al.*, 1999), and the 2.06 Ga Lapland-Karasjok GB (Barnes and Often, 1990;
594 Hanski *et al.*, 2001). Due to the rather wide distribution and specific geochemical features of

595 these lavas, (Barley *et al.*, 2000) coined the term Karasjok-type komatiites after the locality in
596 Norway, where they were first described by (Barnes and Often, 1990).

597 The majority of models that explain the origin of the Karasjok-type komatiites (Capdevila
598 *et al.*, 1999; Tomlinson *et al.*, 1999; Barley *et al.*, 2000) involve deep, high-degree anhydrous
599 melting in mantle plumes in equilibrium with residual majorite garnet, typical of the Al-
600 depleted komatiites (Ohtani, 1984; Herzberg and Ohtani, 1988; Ohtani, 1990). This model is
601 consistent with the estimates of the pressure of melting for the BCF to be between 10 and 14
602 GPa (Herzberg and O'Hara, 2002), which is similar to that for the Barberton komatiites. In
603 order to explain the variable enrichments in Fe and Ti of the Karasjok-type komatiites,
604 (Hanski *et al.*, 2001) proposed that they were derived from a mantle plume source that was
605 heterogeneous, likely because it contained variable, but small amounts of recycled eclogite.

606 (Arndt, 1994) pointed out that the crucial feature that distinguishes komatiites from
607 picrites is the presence of spinifex texture in the former. This feature owes its origin to the
608 early history of komatiite magmas as superheated liquids that picritic magmas are lacking
609 altogether, which, in turn, stems from the extremely high temperature as the defining feature
610 of the komatiite source. (Donaldson, 1979) and (Lofgren, 1983) have shown experimentally
611 that a period of superheating strongly influences the subsequent crystallization history of a
612 silicate liquid. The process of heating a silicate melt well above its liquidus breaks down the
613 structure of the liquid, destroying the chains and networks that act as nuclei during
614 crystallization on subsequent cooling. A liquid subjected to superheating crystallizes quite
615 differently from one that was never superheated. Superheated liquids display a reluctance to
616 nucleate when cooled and the crystals that do form tend to be few, large and skeletal.
617 Komatiite magma follows a path through the mantle that takes it to temperatures well above
618 the liquidus. The period of superheating has the effect that nucleation is inhibited, relatively

619 few phenocrysts form, and heterogeneous nucleation on quenched margins is favored;
620 spinifex texture is the consequence.

621 Contrary to their earlier study, (Stone *et al.*, 1995a), while acknowledging the close spatial
622 and temporal association of the BCF with komatiites from the Abitibi greenstone belt, likely
623 indicating their origin in a hot mantle, proposed that the parental magma that gave rise to the
624 BCF was a ferropicrite with <18% MgO. According to these authors, the geochemistry of the
625 BCF can be explained by a two-source-component mixing model. The first source component
626 was peridotite depleted by extraction of melt prior to generation of the BCF magma, whereas
627 the second one was highly enriched small-degree melt fractions formed in the majorite
628 stability field in the mantle. Mixing of the two source components was proposed to have
629 occurred immediately prior to melting to maintain the radiogenic Nd isotopic composition.

630 In this study, we consider the BCF to be komatiitic in origin based on their textural and
631 chemical features and close spatial and temporal association with the Al-undepleted (Munro
632 Township: (Arndt *et al.*, 1977; Arndt and Nesbitt, 1984; Arndt, 1986) and Al-depleted
633 (Newton Township: (Cattell and Arndt, 1987) komatiites. Following the conventional model
634 for the origin of the Karasjok-type komatiites (Capdevila *et al.*, 1999; Tomlinson *et al.*, 1999;
635 Barley *et al.*, 2000), we consider the parental magma to the BCF to be a product of relatively
636 high-degree partial melting of a melt-depleted, but Fe- and Ti-enriched source. Melting
637 started deep (300-420 km) in the mantle in the majorite stability field based on the estimates
638 of (Herzberg and O'Hara, 2002), which resulted in the strong Al-depleted signature of the
639 parental melt. According to (Herzberg, 1992), Al-depleted komatiitic parental melts that
640 formed under such conditions were derived by high degrees (~50%) of pseudo-invariant
641 melting (L + Ol + Gt + Cpx) of fertile mantle peridotite in the 80- to 100-kbar range, about
642 260- to 330- km depth. The enrichment in incompatible lithophile trace elements could have
643 resulted from mixing of the parental komatiitic magma with low-degree partial melts derived

644 from the same heterogeneous plume; this type of magma mixing and enrichment has been
645 previously advocated for komatiites from Munro and Newton Townships, Ontario (Arndt and
646 Nesbitt, 1984; Cattell and Arndt, 1987). Following this train of logic, we also assume that the
647 parental magma to the BCF had a MgO content similar to the other Al-depleted komatiites in
648 the area, *i.e.*, it contained 25–27 wt. % MgO (Cattell and Arndt, 1987); this parental magma
649 fractionated olivine *en route* to the surface to reach ~16 wt. % MgO upon emplacement.

650 **5.2. HSE systematics of the Boston Creek Flow mantle source**

651 The absolute and relative abundances of HSE in the mantle bear on such key topics as
652 core-mantle differentiation, late-stage planetary accretion and subsequent core-mantle
653 exchange. Here, we use the initial $^{187}\text{Os}/^{188}\text{Os}$ ratio obtained for the BCF to calculate the time-
654 integrated Re/Os in its mantle source by assuming generation of this mantle source soon after
655 Solar System formation. It is estimated, therefore, that this source would have evolved from
656 the Solar System initial $^{187}\text{Os}/^{188}\text{Os} = 0.0952 \pm 2$ at 4568 Ma (Day *et al.*, 2016) to the initial
657 $^{187}\text{Os}/^{188}\text{Os} = 0.10846 \pm 36$ at 2720 Ma with a time-integrated $^{187}\text{Re}/^{188}\text{Os} = 0.404 \pm 11$. This
658 ratio is well within the range observed for chondritic meteorites (average $^{187}\text{Re}/^{188}\text{Os} =$
659 0.410 ± 51 (2SD), as compiled from the data of (Walker *et al.*, 2002; Brandon *et al.*, 2005;
660 Fischer-Gödde *et al.*, 2010). The calculated initial $^{187}\text{Os}/^{188}\text{Os}$ of the BCF source is also well
661 within the range of those for the majority of Archean komatiite systems, as evidenced by a
662 compilation of $^{187}\text{Os}/^{188}\text{Os}$ isotopic data for Archean komatiites (Fig. 10).

663 As has been discussed previously (Puchtel *et al.*, 2016b), more than 90% of the HSE
664 budget of the mantle resides in two types of sulfides (Alard *et al.*, 2000; Lorand and Alard,
665 2001; Luguet *et al.*, 2007). The high-temperature Os-Ir-Ru-rich Fe-Ni monosulfide solid
666 solution (*mss*) forms rounded inclusions in olivine, whereas low-temperature, irregular-
667 shaped Cu-Ni sulfides occupy intergranular space. During partial melting of mantle peridotite,
668 Cu-Ni sulfides enter the melt, whereas the *mss* remains trapped in the melting residue until the

669 degree of melting reaches 20-25% (Barnes *et al.*, 1985; Keays, 1995; Luguet *et al.*, 2007;
670 Fonseca *et al.*, 2011; Fonseca *et al.*, 2012), at which point all the low-temperature sulfide in
671 the residue gets consumed and, as the degree of melting continues to increase, the magma
672 becomes sulfide-undersaturated. It has also recently been shown that decrease in $f\text{S}_2$ with
673 increase in degree of melting triggers exsolution of Os-Ir alloys from the refractory mss in the
674 residue (Fonseca *et al.*, 2011; Fonseca *et al.*, 2012). All low-degree (basalts) and the majority
675 of higher-degree (picrites and komatiites) partial melts are characterized by compatible
676 behavior of Os and Ir during magmatic differentiation, indicating that their parental magmas
677 remained saturated in Os-Ir alloys (Puchtel *et al.*, 2004b; Barnes and Fiorentini, 2008).
678 However, some lavas, such as the 2.8 Ga Kostomuksha and the 3.55 Ga Schapenburg
679 komatiites, exhibit incompatible behavior of Os and Ir during magma differentiation, likely
680 indicating near-complete exhaustion of Os-Ir alloys in the mantle sources of these komatiites
681 (Puchtel and Humayun, 2005; Puchtel *et al.*, 2009a).

682 In order to calculate the absolute HSE abundances in the mantle source of the BCF, the
683 projection technique of (Puchtel *et al.*, 2004b), subsequently modified by (Puchtel *et al.*,
684 2016b) to be applicable to komatiitic lavas derived from parental magmas that experienced
685 fractional crystallization *en route* to the surface, and the HSE abundances in the BCF obtained
686 in this study, were used. Due to the poorly constrained differentiation history of the BCF
687 magma prior to emplacement in terms of Os, Ir, and Ru fractionation, and mobile post-
688 emplacement behavior of Re, only abundances of the incompatible and immobile elements Pt
689 and Pd in the BCF source could be estimated with a sufficiently high degree of accuracy.

690 One of the pre-requisites for this protocol to be applicable is the complete exhaustion of
691 low-temperature sulfides harboring Pt and Pd in the mantle source during partial melting.
692 Based to the models of magma generation for Karasjok-type komatiites (Capdevila *et al.*,
693 1999; Tomlinson *et al.*, 1999; Barley *et al.*, 2000) and following estimates of (Herzberg and

694 O'Hara, 2002) for the depth of the BCF magma generation (300-420 km), in equilibrium with
695 residual majorite garnet, the BCF parental magma was estimated to have formed via moderate
696 to high degrees (>25%) of partial melting of an already melt-depleted source in a mantle
697 plume and, therefore, must have been sulfide undersaturated prior to emplacement. According
698 to (Herzberg, 1992), Al-depleted komatiitic parental melts that form under such conditions
699 were derived by high degrees (~50%) of pseudo-invariant melting ($L + Ol + Gt + Cpx$) of
700 fertile mantle peridotite in the 80- to 100-kbar range, about 260- to 330- km depth; as such,
701 the 25% degree partial melting is likely the minimum estimate. The strongest evidence for the
702 sulfide-undersaturated nature of the BCF is provided by the incompatible behavior of Pd
703 during differentiation. Palladium abundances across the BCF plot on an olivine control line in
704 MgO–Pd space (Fig. 6), indicating that sulfide liquid was not a fractionating phase within the
705 compositional range represented by the samples of this study.

706 It should be noted, however, that the sulfur content at saturation of a mafic magma
707 increases with decreasing pressure, so magmas may become undersaturated during adiabatic
708 ascent (Mavrogenes and O'Neill, 1999). This limitation can only be relaxed if there are no
709 sulfides left in the source after melt separates from the residue, which can only be attained if
710 the degree of melting exceeds ~20-25%, as discussed earlier (Fonseca *et al.*, 2011; Fonseca *et*
711 *al.*, 2012). This degree of melting is lower than estimated for the formation of the BCF
712 parental melt. In addition, at temperatures and pressures of komatiite formation, sulfur
713 becomes even more soluble, and komatiite sources become S-undersaturated at even lower
714 degrees of partial melting (Barnes and Fiorentini, 2008).

715 The first step in calculating the Pt and Pd abundances in the BCF mantle source is to
716 establish the original liquid lines of descent for this komatiitic basalt system. For incompatible
717 Pt and Pd, these liquid lines of descent should pass through the composition of the liquidus
718 olivine that was in equilibrium with the parental komatiite magma with ~27 wt. % MgO, and

719 the composition of the BCF emplaced lava, which resulted from fractionation of this liquidus
720 olivine from the parental komatiite magma. For the present calculations, the Pt and Pd
721 abundances and MgO content of the Pyke Hill komatiitic olivine from (Puchtel *et al.*, 2009b)
722 were used. This choice was based on the assumption that a komatiitic magma similar in MgO
723 content to that at Pyke Hill most likely was the parental magma to the BCF (see the
724 discussion above). Besides, since both Pt and Pd are highly incompatible in olivine (*e.g.*,
725 (Brenan *et al.*, 2003), small variations in the abundances of these elements in the olivine
726 would have had negligible effect on the calculated Pt and Pd abundances in the BCF mantle
727 source. Using the above assumptions and ISOPLOT regression analysis to project the
728 abundances of Pt and Pd measured in the spinifex-textured samples of the BCF in this study
729 and in the Pyke Hill olivine from (Puchtel *et al.*, 2004b), to mantle MgO = 38 wt. %., the Pt
730 and Pd abundances in the BCF source were calculated to be 2.4±0.2 and 2.8±0.3 ppb,
731 respectively (2SD, propagated error). From these results, the total Pt and Pd abundances in the
732 BCF source were calculated to be 5.2±0.7 ppb, or 35±5% of those in the estimates for modern
733 BSE of 14.7±2.0 ppb (Becker *et al.*, 2006).

734 The calculated total Pt and Pd abundances in the source of the BCF are plotted as a
735 function of age and compared with those in the sources of other Archean komatiite systems
736 and the BSE (Fig. 11). The calculated total Pt and Pd abundances in the source of the BCF are
737 substantially lower than those in any of the late Archean komatiite systems studied to-date,
738 which range from 57±4% in the 2.69 Ga Belingwe to 86±6% in the 2.72 Ga Alexo systems,
739 relative to those in the estimates for modern BSE. The only komatiite system with lower total
740 Pt and Pd abundances is 3.55 Ga Schapenburg with 29±5%.

741 **5.2. Origin of the positive ^{182}W anomaly**

742 The first issue to address before discussing the significance of the positive ^{182}W anomaly
743 is the origin of W in the BCF and whether or not it is representative of its mantle source. On a

744 BSE-normalized plot (Fig. 3), W abundances are characterized by variable positive offsets,
745 relative to Th and U, the lithophile trace elements with similar incompatibility during mantle
746 melting under redox conditions close to the FMQ buffer (König *et al.*, 2011). Further, W
747 abundances plot on a trend versus MgO that is oblique to the olivine control line (Fig. 2). This
748 most likely indicates W disturbance during seafloor alteration and/or metamorphism. This
749 conclusion is further confirmed by the positive correlation between indices of alteration, *i.e.*,
750 loss on ignition (LOI), and W/W*, *i.e.*, the magnitude of the W abundance offset relative to U
751 and Th (Fig. 3b). At the same time, there is a negative correlation between indices of
752 alteration and the magnitude of the positive ^{182}W anomaly (Fig. 3c). Moreover, all samples
753 collected across the BCF show uniformly positive ^{182}W anomalies. These observations
754 suggest that the BCF itself was the source of W in the samples analyzed. It should be noted,
755 however, that no negative W/W* abundance anomalies have been found in any samples
756 analyzed that would counter-balance the positive W/W* abundance anomalies in the others.
757 This could indicate that the BCF parental melt has originally been enriched in W. Recently,
758 (Babechuk *et al.*, 2010) have found that many of the highly depleted mantle peridotites
759 contain far higher W concentrations than expected based on the abundances of similarly
760 incompatible lithophile trace elements, such as Th and U. In the absence of convincing
761 indications for alteration, re-enrichment or contamination, these authors concluded that the W
762 excess was caused by retention of W in an Os–Ir alloy phase. During high-degree partial
763 melting involved in komatiite formation, a significant proportion of the Os-Ir alloy that was
764 retained in the mantle source during extraction of low-degree melts would have entered the
765 komatiite melt, resulting in its enrichment in W relative to Th and U. This would be consistent
766 with the enrichment in W in the cumulate zone of the BCF that is also enriched in Os and Ir
767 relative to the spinifex zone. As such, we conclude that the W isotopic composition obtained
768 for the BCF can be considered to be that of the mantle source of the BCF.

769 The ^{182}Hf - ^{182}W isotopic system ($t_{1/2} = 8.9$ Ma) has been commonly used in
770 cosmochemistry to constrain the timing of metal-silicate segregation (Kleine *et al.*, 2002;
771 Kleine *et al.*, 2004a; Kleine *et al.*, 2004b; Touboul *et al.*, 2007; Kleine *et al.*, 2009; Touboul
772 *et al.*, 2015). This is due to the fact that Hf is strongly lithophile, while W is moderately
773 siderophile, and both elements are highly refractory. Thus, Hf is fractionated from W during
774 metal-silicate differentiation, such as that occurring during planetary core segregation. In
775 addition to cosmochemical applications, studies of terrestrial rocks spanning the history of
776 Earth's rock record have documented both positive and negative ^{182}W anomalies (Willbold *et*
777 *al.*, 2011; Touboul *et al.*, 2012; Touboul *et al.*, 2014; Willbold *et al.*, 2015; Puchtel *et al.*,
778 2016a; Puchtel *et al.*, 2016b; Rizo *et al.*, 2016a; Rizo *et al.*, 2016b; Dale *et al.*, 2017; Mundl
779 *et al.*, 2017). These isotopic anomalies have been interpreted within the framework of three
780 broad categories of processes.

781 The first category is core-mantle interaction. Assuming chondritic $^{182}\text{W}/^{184}\text{W}$ for bulk
782 Earth (*i.e.*, $\mu^{182}\text{W} = -190 \pm 10$: (Kleine *et al.*, 2002; Schoenberg *et al.*, 2002; Yin *et al.*, 2002;
783 Kleine *et al.*, 2004a), 13 ppb W for BSE (Arevalo and McDonough, 2008; König *et al.*, 2011)
784 and 590 ppb W for the core (McDonough, 2004), mass balance calculations require the core
785 to have a $\mu^{182}\text{W}$ of ~ -220 to balance the more radiogenic isotopic composition of the BSE
786 ($\mu^{182}\text{W} = 0$). Addition of core metal to a mantle domain would, therefore, lead to a decrease in
787 the $\mu^{182}\text{W}$ value of that mantle domain.

788 The second category capable of generating ^{182}W heterogeneity in the mantle is metal-
789 silicate or silicate-silicate fractionation processes that operated within the first ~ 50 Ma of
790 Solar System history, while ^{182}Hf was still extant (*e.g.*, (Touboul *et al.*, 2012). Metal-silicate
791 fractionation, followed by removal of the metal from an isolated mantle domain, such as a
792 basal magma ocean, would leave the silicate domain with suprachondritic Hf/W, due to
793 preferential partitioning of W into the metal. Alternatively, crystal-liquid fractionation in a

794 purely silicate system, such as a global magma ocean, would lead to high Hf/W in early
795 formed cumulates and low Hf/W in the residual liquid, due to the more incompatible nature of
796 W compared with Hf. If any of these fractionation processes occurred while ^{182}Hf was still
797 extant, excesses in ^{182}W would eventually be created in both the silicates left after metal
798 segregation and the silicate cumulates in the differentiated primordial magma ocean. By
799 contrast, a complementary residual magma ocean liquid would develop deficits in ^{182}W ,
800 compared to the ambient mantle.

801 The third category is disproportional late accretion (Willbold *et al.*, 2011; Kruijer *et al.*,
802 2015; Touboul *et al.*, 2015; Willbold *et al.*, 2015). Late accretion is a process commonly
803 proposed to account for high absolute, and chondritic relative abundances of HSE in the
804 modern mantle (Kimura *et al.*, 1974; Morgan *et al.*, 1981; Chou *et al.*, 1983). It requires
805 addition to the mantle of ~0.5 wt. % of Earth's mass (Walker, 2009) of HSE-rich
806 planetesimals with chondritic bulk compositions after last equilibration between the core and
807 mantle. Chondrites have ~20 times higher W abundances and -190 ± 10 ppm less radiogenic
808 $^{182}\text{W}/^{184}\text{W}$ than the modern terrestrial mantle (Kleine *et al.*, 2002; Schoenberg *et al.*, 2002;
809 Yin *et al.*, 2002; Kleine *et al.*, 2004a); as a result, late accretion likely led to a decrease in the
810 $^{182}\text{W}/^{184}\text{W}$ ratio of the mantle by ~25 ppm compared to the pre-late accretionary mantle. The
811 fact that the $^{182}\text{W}/^{184}\text{W}$ of the HSE-poor lunar mantle is ~ 25 ppm higher than BSE provides
812 supporting evidence for this process (Kruijer *et al.*, 2015; Touboul *et al.*, 2015). Thus, any
813 mantle domain to which less of a late accretionary component was added, would be $^{182}\text{W}-$
814 enriched, compared to the mantle to which a full complement of late accretionary component
815 was added. Such a mantle domain would also be expected to be depleted in HSE, compared to
816 BSE.

817 The positive ^{182}W anomaly observed in the BCF cannot be the result of core-mantle
818 interaction, as this process would decrease, rather than increase, $^{182}\text{W}/^{184}\text{W}$ in the mantle

819 source of the BCF. In addition, core-mantle interaction would have increased the HSE
820 abundances in the BCF source over ambient mantle levels, whereas the BCF mantle domain is
821 estimated to contain only ~35% of the total HSE complement of the BSE.

822 Crystal-liquid fractionation in a global magma ocean could have created cumulate-rich
823 mantle domains with high Hf/W ratios that over a short period of time would have grown in
824 excesses of ^{182}W ; i.e., led to a positive $\mu^{182}\text{W}$ anomaly, just as observed in the BCF. However,
825 early crystal-liquid fractionation would also have resulted in fractionation of the Sm/Nd ratio
826 and, as a result, the creation of a positive ^{142}Nd anomaly complementary to the positive ^{182}W
827 anomaly in the early magma ocean cumulates. Such an anomaly is not observed. In addition,
828 unlike early Archean komatiite systems, the generation of which have been evoked to involve
829 early magma ocean processes, partly owing to decoupled, or incongruent, Nd-Hf isotope
830 systematics (Puchtel *et al.*, 2013; Puchtel *et al.*, 2016a), the BCF lavas plot on the terrestrial
831 Nd-Hf array, suggesting minimal involvement of early magma ocean processes in the
832 fractionation of the lithophile trace elements in the BCF mantle source (Fig. 8).

833 Metal-silicate fractionation, followed by removal of the metal from a basal magma ocean,
834 would have fractionated the Hf/W ratio, and would have had no collateral effect on the
835 Sm/Nd ratio and, therefore, neither on the ^{146}Sm - ^{142}Nd systematics. Moreover, subsequent
836 removal of the metal from the basal magma ocean would have driven the HSE abundances in
837 the source of the BCF in the observed direction, i.e., towards the sub-BSE levels. This process
838 would be equivalent in its net effect to the core formation event that occurred within the first
839 30 Ma of Solar System history (*e.g.*, (Yin *et al.*, 2002) and that have quantitatively stripped
840 the mantle of HSE. However, this process would also have fractionated the Re/Os ratio in the
841 mantle domain, that gave rise to the BCF, away from the chondritic value (*e.g.*, (Touboul *et*
842 *al.*, 2012), which is not observed.

843 We conclude, therefore, that disproportional late accretion is the best explanation for the
844 observed positive ^{182}W anomaly in the BCF. If late accreted materials were not rapidly mixed
845 and homogenized throughout the mantle, as seems likely to have been the case in the context
846 of the so-called stochastic late accretion (Bottke et al., 2010), where late accreted material
847 consisted of a few large (up to 3,000 km in diameter) planetesimals, then portions of the
848 mantle would be expected to initially have both excesses and deficits of late accreted
849 materials, compared to the average amount required to accommodate the HSE budget of the
850 BSE (e.g., (Willbold et al., 2011; Willbold et al., 2015)).

851 In order to evaluate the effect of disproportional late accretion on the ^{182}W and HSE
852 systematics, we plotted the $\mu^{182}\text{W}$ in the BCF versus the total calculated Pt and Pd
853 abundances in its mantle source relative to those in the present-day BSE (Fig. 12). This
854 proportion corresponds to the fraction of the total HSE budget of the BSE added during late
855 accretion assuming an HSE-free mantle following core formation. The W isotopic
856 composition of the BSE prior to late accretion is constrained by the $^{182}\text{W}/^{184}\text{W}$ data for the
857 lunar mantle to be $+25\pm5$ ppm (Kruijer et al., 2015; Touboul et al., 2015; Kruijer and Kleine,
858 2017). Our calculations indicate that, when the full uncertainties on the W isotopic
859 composition of the BCF source and the pre-late accretion mantle are considered, the observed
860 11.5 ± 4.5 ppm enrichment in ^{182}W would be achieved in a mantle domain to which $48\pm28\%$ of
861 late accreted materials, with chondritic W isotopic compositions, were added, relative to the
862 present-day BSE. This is consistent with the calculated total HSE abundances in the source of
863 the BCF of $35\pm5\%$ of those in the estimates for the present-day BSE. At the same time,
864 addition of even full complement of late accreted chondritic material with similar Nd
865 abundance and negative $\mu^{142}\text{Nd}$ to the mantle will have negligible effect on both the Nd
866 budget of the mantle and its Nd isotopic composition. We conclude, therefore, that stochastic
867 late accretion, with incomplete mixing between mantle domains enriched and not enriched in

868 late accreted components, is the most plausible mechanism for the formation of the observed
869 short- and long-lived isotopic and elemental systematics in the mantle domain that gave rise
870 to the BCF. This mantle domain must have remained isolated from the rest of the convecting
871 mantle at least until the formation of the BCF at 2.72 Ga, implying a long time scale for
872 mixing of the terrestrial mantle, on the order of at least 1.8 billion years.

873 The predominant giant impact model of lunar formation requires the Moon to consist
874 mainly of the material of the impactor (e.g., (Canup and Asphaug, 2001; Canup, 2004), which
875 poses significant problems for this model in light of similarities of O, Si, and Ti isotopic
876 compositions of the two planetary bodies (e.g., (Dauphas *et al.*, 2014). More recent dynamic
877 models (e.g., (Canup, 2012), however, are more permissible of the formation of the Moon
878 from the material of the Earth's mantle. This controversy can be addressed using the data of
879 the present study. It can be expected that, if the ^{182}W excess in the BCF is attributed to the
880 deficit of late accreted component in its mantle source alone, and if the ^{182}W composition of
881 the lunar mantle largely corresponds to the ^{182}W composition of pre-late accretion BSE, the
882 present day BSE, lunar mantle and the BCF source would plot on the single trend line in
883 Figure 12. To test this hypothesis, we have performed ISOPLOT regression analysis using
884 ± 4.5 ppm as the uncertainty on both modern BSE and BCF source ^{182}W compositions and
885 $\pm 5\%$ (absolute) as an uncertainty on the modern BSE and BCF source total HSE abundances.
886 The results of the regression analysis indicate that the calculated pre-late accretion BSE had
887 an ^{182}W excess of 18 ± 7 ppm. This result is identical to the independently estimated ^{182}W
888 isotopic composition of the BSE of 18 ± 9 by (Kleine and Walker, 2017). It is also identical to
889 the estimates for the ^{182}W composition of the Moon of $+25 \pm 5$ ppm, thus, providing further
890 support to the notion that the Moon and Earth formed from material with identical ^{182}W
891 compositions (Kleine and Walker, 2017).

892 **5.3. Mechanisms of isolation of late accreted materials in the mantle**

893 It is estimated, based on the studies of HSE abundances and Re-Os isotope systematics in
894 terrestrial mantle samples (Meisel *et al.*, 2001; Becker *et al.*, 2006; Fischer-Gödde *et al.*,
895 2011) and derivative mantle melts from the martian (Brandon *et al.*, 2012) and lunar (Warren
896 *et al.*, 1989; Ringwood, 1992; Righter *et al.*, 2000; Walker *et al.*, 2004; Day *et al.*, 2007; Day
897 and Walker, 2015) mantles that the mass ratio of late accreted materials for the three bodies
898 was ~1:10:1200. However, the Earth/Moon impact number flux ratio for both late accreted
899 planetesimals and present-day near-Earth objects is ~20, with this value being a reflection of
900 different gravitational cross sectional areas of the two bodies (Bottke *et al.*, 2007). It was
901 concluded, therefore, to be highly unlikely that numerous, small projectiles could have
902 achieved an Earth/Moon mass influx ratio close to 1200, especially in the aftermath of the
903 Moon-forming event, when most leftover planetesimals and asteroids in the inner Solar
904 System were dynamically excited (Bottke *et al.*, 2002; Bottke *et al.*, 2007).

905 It is also likely that most HSE were delivered to the terrestrial, martian, and lunar mantles
906 within ~200 Ma of core formation termination on Earth. This is due to the fact that the lunar
907 crust, which formed between 4.34 and 4.37 Ga (Borg *et al.*, 2014), is essentially intact and has
908 only been modestly contaminated by extra-lunar materials (*e.g.*, (Morgan *et al.*, 1977;
909 Norman *et al.*, 2002; Warren, 2003; Norman, 2005; Puchtel *et al.*, 2008; Fischer-Gödde and
910 Becker, 2012). It has also been argued, based on the ^{142}Nd , ^{182}W , Re-Pt-Os, and HSE
911 abundance data, that the 3.26-3.55 Ga Barberton komatiites (Puchtel *et al.*, 2014; Puchtel *et*
912 *al.*, 2016a), 3.6-3.8 Inukjuak supracrustal rocks (Caro *et al.*, 2017), 3.8-4.3 Ga Isua
913 supracrustal belt and the Nuvvuagittuq greenstone belt rocks (O'Neil *et al.*, 2016), as well as
914 the 2.82 Ga Kostomuksha komatiites (Touboul *et al.*, 2012), were derived from mantle
915 domains that were isolated from the rest of the mantle prior to ~4.40 Ga. On Mars, magma
916 ocean crystallization and crust formation most likely occurred within 40 Ma of the Solar
917 System history based on the combined ^{182}W - ^{142}Nd systematics of a comprehensive suite of

918 martian meteorites (Kruijer *et al.*, 2017). This implies that most HSEs were delivered by
919 leftover debris from terrestrial planet accretion, which was probably dominated by stony
920 and/or differentiated planetesimals (Becker *et al.*, 2006). These materials have high rate of
921 mass retention on impact and, therefore, should not bias the estimated mass ratio of late
922 accreted materials for the Earth/Mars/Moon system. Based on the best results of Monte-Carlo
923 code simulation (Bottke *et al.*, 2010), the HSE were delivered to the Earth and Moon systems
924 via a few large projectiles with mean diameters of 2500 to 3000 km and 250 to 300 km,
925 respectively. This is also consistent with the observation that, in the absence of plate
926 tectonics, the impactors needed to be large enough to breach early planetary lithosphere,
927 create local magma ponds or lakes from their impact energy, and then efficiently mix into the
928 mantle, but not so large that their impact-fragmented cores coalesced with the Earth's core
929 (Dahl and Stevenson, 2010). Assuming Earth to be in a magma ocean phase at the time of the
930 impact, the iron core of a differentiated projectile that is assumed to be half of the projectile's
931 diameter, will likely become emulsified into the mantle if it is smaller than the depth of the
932 magma ocean (Bottke *et al.*, 2010; Dahl and Stevenson, 2010). For Earth, this criterion limits
933 HSE delivery among differentiated projectiles to diameters <4000 km (Rubie *et al.*, 2003).

934 The differentiated projectiles would likely consist of HSE-rich cores and HSE-stripped
935 silicate mantles. Upon impact, the cores will likely emulsify in a magma ocean, whereas the
936 silicate mantles will not. As a result, domains with low HSE abundances and positive ^{182}W
937 anomalies would be expected to have been created. In the absence of modern-style plate
938 tectonics, the silicate domains would likely have survived for extended periods of time before
939 being homogenized within the mantle via whole-mantle convection. This model, which
940 requires delivery of the bulk of late accreted materials prior to 4.40 Ga, is consistent with the
941 observation of an absence of trend of increasing HSE abundances in komatiitic sources from

942 3.5 to 2.7 Ga. It is also consistent with the large, non-systematic variations in HSE
943 abundances between individual both early and late Archean komatiite systems (Fig. 11).
944 A stagnant, or episodic, subduction regime in the Hadean is consistent with the available
945 observations (O'Neill and Debaille, 2014) and was most likely the mechanism that was
946 responsible for the slow mixing of late accreted materials into the mantle. These observations
947 include mantle mixing constraints (long residence time of isotope anomalies and
948 compositional heterogeneities) and thermal history models (higher rates of internal heat
949 production versus lower heat flux to avoid the “Archean thermal catastrophe”). These also
950 include basic geologic data, such as formation of early Archean TTGs and presence of
951 greenstone sequences with interleaving island arc and plume-derived lavas. It can explain the
952 worldwide preservation of ^{142}Nd anomalies in the 4.2-2.7 Ga geological record and their
953 complete disappearance in the post-Archean (Debaille *et al.*, 2013). Apparently, W isotope
954 heterogeneities were more resilient to the mantle homogenization processes compared to
955 those of Nd, as evidenced by the presence of large ^{182}W anomalies in recent and modern
956 plume-derived lavas (Rizo *et al.*, 2016a; Mundl *et al.*, 2017); this could be due to the different
957 nature of these heterogeneities, as well as different location of their respective mantle sources.

958 **6. Conclusions**

959 The 2.72 Ga Boston Creek komatiitic basalt lava flow (BCF) in the Abitibi greenstone
960 belt is characterized by a positive ^{182}W anomaly, chondritic $^{187}\text{Os}/^{188}\text{Os}$ isotopic composition
961 and low calculated absolute HSE abundances in its mantle source, a set of geochemical
962 features that are collectively unique among the komatiite systems studied so far. When
963 considered together, these constraints require derivation of the parental BCF magma from a
964 mantle source that formed very early in Earth’s history and received only a fraction of the
965 present-day mantle HSE complement before becoming isolated until the time of komatiite
966 emplacement. These data provide new evidence for the highly heterogeneous nature of the

967 Archean mantle in terms of absolute HSE abundances, consistent with stochastic late
968 accretion of a limited number of sizable impactors into the mantle. The survival of the early-
969 formed BCF mantle source for \geq 1.8 billion years implies that portions of the mantle remained
970 poorly mixed with regard to HSE and W until at least the late Archean.

971

972 **Acknowledgements**

973 This work was supported by NSF Petrology and Geochemistry grant EAR 1447174 to
974 ISP, NSF-CSEDI grant EAR 1265169 to RJW, ANR grant ANR-10-BLANC-0603 M&Ms –
975 Mantle Melting – Measurements, Models, Mechanisms to JBT, and NSF-IF grant EAR
976 0549300, which provided partial support for the *Triton* mass-spectrometer used for most of
977 the measurements in this study. We are grateful to Valentina Puchtel and Richard Ash for
978 help with preparation of samples and ICP-MS measurements at the *IGL* and *PL*, and to
979 Philippe Telouk for maintenance of the MC-ICP-MS in Lyon. Mike Lesher is thanked for
980 guidance during field work in the Kirkland Lake area.

981

982 **References**

- 983 Alard, O., Griffin, W.L., Lorand, J.-P., Jackson, S.E., and O'Reilly, S.Y., 2000. Non-
984 chondritic distribution of the highly siderophile elements in mantle sulfides. *Nature*
985 **407**(6806): 891-894.
- 986 Archer, G.J., Mundl, A., Walker, R.J., Worsham, E.A., and Bermingham, K.R., 2017. High-
987 precision analysis of $^{182}\text{W}/^{184}\text{W}$ and $^{183}\text{W}/^{184}\text{W}$ by negative thermal ionization mass
988 spectrometry: Per-integration oxide corrections using measured $^{18}\text{O}/^{16}\text{O}$.
989 *INTERNATIONAL JOURNAL OF MASS SPECTROMETRY* **414**: 80-86.
- 990 Arevalo, R., and McDonough, W.F., 2008. Tungsten geochemistry and implications for
991 understanding the Earth's interior. *Earth and Planetary Science Letters* **272**(3-4): 656-
992 665.
- 993 Arndt, N.T., 1977. Thick, layered peridotite-gabbro lava flows in Munro Township, Ontario.
994 *Canadian Journal of Earth Sciences* **14**(11): 2620-2637.
- 995 Arndt, N.T., 1986. Differentiation of komatiite flows. *Journal of Petrology* **27**(2): 279-301.
- 996 Arndt, N.T. (1994). Archean komatiites. *Archean Crustal Evolution*. Condie, K.C.
997 Amsterdam, Elsevier: 11-44.
- 998 Arndt, N.T., Lesher, C.M., and Barnes, S.J. (2008). Komatiite. Cambridge, UK, Cambridge
999 University Press.
- 1000 Arndt, N.T., Naldrett, A.J., and Pyke, D.R., 1977. Komatiitic and iron-rich tholeiitic lavas of
1001 Munro Township, northeast Ontario. *Journal of Petrology* **18**: 319-369.
- 1002 Arndt, N.T., and Nesbitt, R.W. (1984). Magma mixing in komatiitic lavas from Munro
1003 Township, Ontario. *Archaeon Geochemistry*. Kröner, A. Berlin-Heidelberg: 99-114.
- 1004 Babechuk, M.G., Kamber, B.S., Greig, A., Canil, D., and Kodolanyi, J., 2010. The behaviour
1005 of tungsten during mantle melting revisited with implications for planetary
1006 differentiation time scales. *Geochimica et Cosmochimica Acta* **74**(4): 1448-1470.
- 1007 Barley, M.E., Kerrich, R., Reudavy, I., and Xie, Q., 2000. Late Archaean Ti-rich, Al-depleted
1008 komatiites and komatiitic volcaniclastic rocks from the Murchison Terrane in Western
1009 Australia. *Australian Journal of Earth Sciences* **47**(5): 873-883.
- 1010 Barnes, S.-J., Naldrett, A.J., and Gorton, M.P., 1985. The origin of the fractionation of
1011 platinum-group elements in terrestrial magmas. *Chemical Geology* **53**(3-4): 303-323.
- 1012 Barnes, S.-J., and Often, M., 1990. Ti-rich komatiites from Northern Norway. *Contributions
1013 to Mineralogy and Petrology* **105**(1): 42-54.
- 1014 Barnes, S.J., and Fiorentini, M.L., 2008. Iridium, ruthenium and rhodium in komatiites:
1015 Evidence for iridium alloy saturation. *Chemical Geology* **257**(1-2): 44-58.
- 1016 Becker, H., Horan, M.F., Walker, R.J., Gao, S., Lorand, J.-P., and Rudnick, R.L., 2006.
1017 Highly siderophile element composition of the Earth's primitive upper mantle:
1018 Constraints from new data on peridotite massifs and xenoliths. *Geochimica et
1019 Cosmochimica Acta* **70**(17): 4528-4550.
- 1020 Bennett, V.C., Brandon, A.D., and Nutman, A.P., 2007. Coupled $^{142}\text{Nd}-^{143}\text{Nd}$ isotopic
1021 evidence for Hadean mantle dynamics. *Science* **318**(5858): 1907-1910.
- 1022 Birck, J.L., Roy-Barman, M., and Capman, F., 1997. Re-Os isotopic measurements at the
1023 femtomole level in natural samples. *Geostandards Newsletter* **20**(1): 19-27.
- 1024 Blichert-Toft, J., 2001. On the Lu-Hf isotope geochemistry of silicate rocks. *Geostandards
1025 Newsletter-the Journal of Geostandards and Geoanalysis* **25**(1): 41-56.
- 1026 Blichert-Toft, J., and Albarède, F., 1997. The Lu-Hf isotope geochemistry of chondrites and
1027 the evolution of the mantle-crust system. *Earth and Planetary Science Letters* **148**(1-
1028 2): 243-258.

- 1029 Blichert-Toft, J., Boyet, M., Telouk, P., and Albarede, F., 2002. ^{147}Sm - ^{143}Nd and ^{176}Lu - ^{176}Hf
 1030 in eucrites and the differentiation of the HED parent body. *Earth and Planetary*
 1031 *Science Letters* **204**(1-2): 167-181.
- 1032 Blichert-Toft, J., Chauvel, C., and Albaréde, F., 1997. Separation of Hf and Lu for high-
 1033 precision isotope analysis of rock samples by magnetic sector multiple collector ICP-
 1034 MS. *Contributions to Mineralogy and Petrology* **127**(3): 248-260.
- 1035 Blichert-Toft, J., and Puchtel, I.S., 2010. Depleted mantle sources through time: Evidence
 1036 from Lu-Hf and Sm-Nd isotope systematics of Archean komatiites. *Earth and*
 1037 *Planetary Science Letters* **297**(3-4): 598-606.
- 1038 Borg, L.E., Gaffney, A.M., and Shearer, C.K., 2014. A review of lunar chronology revealing
 1039 a preponderance of 4.34–4.37 Ga ages. *Meteoritics and Planetary Science* **50**(4): 715-
 1040 732.
- 1041 Bottke, W.F., Levison, H.F., Nesvorný, D., and Dones, L., 2007. Can planetesimals left over
 1042 from terrestrial planet formation produce the lunar Late Heavy Bombardment? *Icarus*
 1043 **190**(1): 203-223.
- 1044 Bottke, W.F., Morbidelli, A., Jedicke, R., Petit, J.-M., Levison, H.F., Michel, P., and
 1045 Metcalfe, T.S., 2002. Debiased Orbital and Absolute Magnitude Distribution of the
 1046 Near-Earth Objects. *Icarus* **156**(2): 399-433.
- 1047 Bottke, W.F., Walker, R.J., Day, J.M.D., Nesvorný, D., and Elkins-Tanton, L., 2010.
 1048 Stochastic Late Accretion to Earth, the Moon, and Mars. *Science* **330**(6010): 1527-
 1049 1530.
- 1050 Bouvier, A., Vervoort, J.D., and Patchett, P.J., 2008. The Lu-Hf and Sm-Nd isotopic
 1051 composition of CHUR: Constraints from unequilibrated chondrites and implications
 1052 for the bulk composition of terrestrial planets. *Earth and Planetary Science Letters*
 1053 **273**(1-2): 48-57.
- 1054 Boyet, M., Blichert-Toft, J., Rosing, M., Storey, M., Télouk, P., and Albarède, F., 2003. ^{142}Nd
 1055 evidence for early Earth differentiation. *Earth and Planetary Science Letters* **214**: 427-
 1056 442.
- 1057 Boyet, M., and Carlson, R.W., 2005. ^{142}Nd evidence for early (> 4.53 Ga) global
 1058 differentiation of the silicate Earth. *Science* **309**(5734): 576-581.
- 1059 Boyet, M., and Carlson, R.W., 2006. A new geochemical model for the Earth's mantle
 1060 inferred from ^{146}Sm - ^{142}Nd systematics. *Earth and Planetary Science Letters* **250**(1-2):
 1061 254-268.
- 1062 Brandon, A.D., Humayun, M., Puchtel, I.S., and Zolensky, M., 2005. Re-Os isotopic
 1063 systematics and platinum group element composition of the Tagish Lake carbonaceous
 1064 chondrite. *Geochimica et Cosmochimica Acta* **69**(6): 1619-1631.
- 1065 Brandon, A.D., Puchtel, I.S., Walker, R.J., Day, J.M.D., Irving, A.J., and Taylor, L.A., 2012.
 1066 Evolution of the martian mantle Inferred from the ^{187}Re - ^{187}Os isotope and highly
 1067 siderophile element abundance systematics of shergottite meteorites. *Geochimica et*
 1068 *Cosmochimica Acta* **76**(1): 206-235.
- 1069 Brenan, J.M., McDonough, W.F., and Dalpé, C., 2003. Experimental constraints on the
 1070 partitioning of rhenium and some platinum-group elements between olivine and
 1071 silicate melt. *Earth and Planetary Science Letters* **212**(1-2): 135-150.
- 1072 Canup, R.M., 2004. Simulations of a late lunar-forming impact. *Icarus* **168**(2): 433-456.
- 1073 Canup, R.M., 2012. Forming a Moon with an Earth-like Composition via a Giant Impact.
 1074 *Science* **338**(6110): 1052-1055.
- 1075 Canup, R.M., and Asphaug, E., 2001. Origin of the Moon in a giant impact near the end of the
 1076 Earth's formation. *Nature* **412**(6848): 708-712.
- 1077 Capdevila, R., Arndt, N.T., Letendre, J., and Sauvage, J.-F., 1999. Diamonds in volcaniclastic
 1078 komatiite from French Guiana. *Nature* **399**(6735): 456-458.

- 1079 Carlson, R.W., and Boyet, M., 2008. Composition of the Earth's interior: the importance of
1080 early events. *Philosophical Transactions of the Royal Society a-Mathematical Physical*
1081 and Engineering Sciences **366**(1883): 4077-4103.
- 1082 Caro, G., Bourdon, B., Birck, J.-L., and Moorbat, S., 2006. High-precision $^{142}\text{Nd}/^{144}\text{Nd}$
1083 measurements in terrestrial rocks: Constraints on the early differentiation of the
1084 Earth's mantle. *Geochimica et Cosmochimica Acta* **70**(1): 164-191.
- 1085 Caro, G., Bourdon, B., Birck, J.L., and Moorbat, S., 2003. $^{146}\text{Sm}-^{142}\text{Nd}$ evidence from Isua
1086 metamorphosed sediments for early differentiation of the Earth's mantle. *Nature*
1087 **423**(6938): 428-432.
- 1088 Caro, G., Morino, P., Mojzsis, S.J., Cates, N.L., and Bleeker, W., 2017. Sluggish Hadean
1089 geodynamics: Evidence from coupled $^{146,147}\text{Sm}-^{142,143}\text{Nd}$ systematics in Eoarchean
1090 supracrustal rocks of the Inukjuak domain (Québec). *Earth and Planetary Science*
1091 Letters **457**: 23-37.
- 1092 Cattell, A., and Arndt, N.T., 1987. Low- and high-alumina komatiites from a Late Archaean
1093 sequence, Newton Township, Ontario. *Contributions to Mineralogy and Petrology*
1094 **97**(2): 218-227.
- 1095 Chou, C.-L., Shaw, D.M., and Crocket, J.H., 1983. Siderophile trace elements in the Earth's
1096 oceanic crust and upper mantle. *Journal of Geophysical Research* **88**(S2): A507-A518.
- 1097 Cohen, A.S., and Waters, F.G., 1996. Separation of osmium from geological materials by
1098 solvent extraction for analysis by thermal ionisation mass spectrometry. *Analytica*
1099 *Chimica Acta* **332**(2-3): 269-275.
- 1100 Corfu, F., and Noble, S.R., 1992. Genesis of the southern Abitibi greenstone belt, Superior
1101 Province, Canada: Evidence from zircon Hf-isotope analyses using a single filament
1102 technique. *Geochimica et Cosmochimica Acta* **56**(5): 2081-2097.
- 1103 Creaser, R.A., Papanastassiou, D.A., and Wasserburg, G.J., 1991. Negative Thermal Ion
1104 Mass-Spectrometry of Osmium, Rhodium, and Iridium. *Geochimica et Cosmochimica*
1105 *Acta* **55**(1): 397-401.
- 1106 Dahl, T.W., and Stevenson, D.J., 2010. Turbulent mixing of metal and silicate during planet
1107 accretion - And interpretation of the Hf-W chronometer. *Earth and Planetary Science*
1108 Letters **295**(1-2): 177-186.
- 1109 Dale, C.W., Kruijer, T.S., and Burton, K.W., 2017. Highly siderophile element and ^{182}W
1110 evidence for a partial late veneer in the source of 3.8 Ga rocks from Isua, Greenland.
1111 *Earth and Planetary Science Letters* **458**: 394-404.
- 1112 Dale, C.W., Macpherson, C.G., Pearson, D.G., Hammond, S.J., and Arculus, R.J., 2012. Inter-
1113 element fractionation of highly siderophile elements in the Tonga Arc due to flux
1114 melting of a depleted source. *Geochimica et Cosmochimica Acta* **89**(Supplement C):
1115 202-225.
- 1116 Dauphas, N., Burkhardt, C., Warren, P.H., and Fang-Zhen, T., 2014. Geochemical arguments
1117 for an Earth-like Moon-forming impactor. *Philosophical Transactions of the Royal*
1118 *Society A: Mathematical, Physical and Engineering Sciences*
1119 **372**(2024): 20130244.
- 1120 Day, J.M.D., Brandon, A.D., and Walker, R.J., 2016. Highly Siderophile Elements in Earth,
1121 Mars, the Moon, and Asteroids. *Reviews in Mineralogy and Geochemistry* **81**(1): 161-
1122 238.
- 1123 Day, J.M.D., Pearson, D.G., and Taylor, L.A., 2007. Highly siderophile element constraints
1124 on accretion and differentiation of the Earth-Moon system. *Science* **315**(5809): 217-
1125 219.
- 1126 Day, J.M.D., and Walker, R.J., 2015. Highly siderophile element depletion in the Moon. *Earth*
1127 and Planetary Science Letters **423**: 114-124.

- 1128 Debaille, V., O'Neill, C., Brandon, A.D., Haenecour, P., Yin, Q.-Z., Mattielli, N., and
1129 Treiman, A.H., 2013. Stagnant-lid tectonics in early Earth revealed by ^{142}Nd variations
1130 in late Archean rocks. *Earth and Planetary Science Letters* **373**: 83-92.
- 1131 Donaldson, C.H., 1979. An experimental investigation of the delay in nucleation of olivine in
1132 Mafic Magmas. *Contributions to Mineralogy and Petrology* **69**(1): 21-32.
- 1133 Fischer-Gödde, M., and Becker, H., 2012. Osmium isotope and highly siderophile element
1134 constraints on ages and nature of meteoritic components in ancient lunar impact rocks.
1135 *Geochimica et Cosmochimica Acta* **77**: 135-156.
- 1136 Fischer-Gödde, M., Becker, H., and Wombacher, F., 2010. Rhodium, gold and other highly
1137 siderophile element abundances in chondritic meteorites. *Geochimica et*
1138 *Cosmochimica Acta* **74**(1): 356-379.
- 1139 Fischer-Gödde, M., Becker, H., and Wombacher, F., 2011. Rhodium, gold and other highly
1140 siderophile elements in orogenic peridotites and peridotite xenoliths. *Chemical*
1141 *Geology* **280**(3-4): 365-383.
- 1142 Fonseca, R.O.C., Laurenz, V., Mallmann, G., Luguet, A., Hoehne, N., and Jochum, K.P.,
1143 2012. New constraints on the genesis and long-term stability of Os-rich alloys in the
1144 Earth's mantle. *Geochimica et Cosmochimica Acta* **87**: 227-242.
- 1145 Fonseca, R.O.C., Mallmann, G., O'Neill, H.S.C., Campbell, I.H., and Laurenz, V., 2011.
1146 Solubility of Os and Ir in sulfide melt: Implications for Re/Os fractionation during
1147 mantle melting. *Earth and Planetary Science Letters* **311**(3-4): 339-350.
- 1148 Foster, J.G., Lambert, D.D., Frick, L.R., and Maas, R., 1996. Re-Os isotopic evidence for
1149 genesis of Archaean nickel ores from uncontaminated komatiites. *Nature* **382**(6593):
1150 703-706.
- 1151 Green, J.C., and Shulz, K.J., 1977. Iron-rich basaltic komatiites in the Early Precambrian
1152 Vermilion district, Minnesota. *Canadian Journal of Earth Sciences* **14**(10): 2181-2192.
- 1153 Hamilton, P.J., O'Nions, R.K., Bridgwater, D., and Nutman, A.P., 1983. Sm-Nd studies of
1154 Archaean metasediments and metavolcanics from West Greenland and their
1155 implications for the Earth's early history. *Earth and Planetary Science Letters* **62**(2):
1156 263-272.
- 1157 Hanski, E., Huhma, H., Rastas, P., and Kamenetsky, V.S., 2001. The Paleoproterozoic
1158 komatiite-picrite association of Finnish Lapland. *Journal of Petrology* **42**(5): 855-876.
- 1159 Herzberg, C., and O'Hara, M.J., 2002. Plume-associated ultramafic magmas of Phanerozoic
1160 age. *Journal of Petrology* **43**(10): 1857-1883.
- 1161 Herzberg, C.T., 1992. Depth and degree of melting of komatiites. *Journal of Geophysical*
1162 *Research* **97**(B4): 4521-4540.
- 1163 Herzberg, C.T., and Ohtani, E., 1988. Origin of komatiite at high pressures. *Earth and*
1164 *Planetary Science Letters* **88**(3-4): 321-329.
- 1165 Hofmann, A.W., 1988. Chemical differentiation of the Earth: The relationship between
1166 mantle, continental crust and oceanic crust. *Earth and Planetary Science Letters* **90**(3):
1167 297-314.
- 1168 Hollings, P., and Wyman, D., 1999. Trace element and Sm-Nd systematics of volcanic and
1169 intrusive rocks from the 3 Ga Lumby Lake Greenstone belt, Superior Province:
1170 evidence for Archean plume-arc interaction. *Lithos* **46**(2): 189-213.
- 1171 Horan, M.F., Walker, R.J., Morgan, J.W., Grossman, J.N., and Rubin, A.E., 2003. Highly
1172 siderophile elements in chondrites. *Chemical Geology* **196**(1-4): 5-20.
- 1173 Jacobsen, S.B., and Wasserburg, G.J., 1980. Sm-Nd isotopic evolution of chondrites. *Earth*
1174 *and Planetary Science Letters* **50**(1): 139-155.
- 1175 Jensen, L.S., and Pyke, D.R. (1982). Komatiites in the Ontario portion of the Abitibi belt.
1176 Komatiites. Arndt, N.T. and Nisbet, E.G. London, George Allen and Unwin: 147-158.

- 1177 Jolly, W.T., 1980. Development and degradation of Archean lavas, Abitibi area, Canada, in
1178 light of major-element geochemistry. *Journal of Petrology* **21**(2): 323-363.
- 1179 Keays, R.R., 1995. The role of komatiitic and picritic magmatism and S-saturation in the
1180 formation of ore deposits. *Lithos* **34**(1-3): 1-18.
- 1181 Kimura, K., Lewis, R.S., and Anders, S., 1974. Distribution of gold and rhenium between
1182 nickel-iron and silicate melts; implications for abundance of siderophile elements on
1183 the Earth and Moon. *Geochimica et Cosmochimica Acta* **38**(5): 683-701.
- 1184 Kleine, T., Mezger, K., Münker, C., Palme, H., and Bischoff, A., 2004a. ^{182}Hf - ^{182}W isotope
1185 systematics of chondrites, eucrites, and martian meteorites: Chronology of core
1186 formation and early mantle differentiation in Vesta and Mars. *Geochimica et*
1187 *Cosmochimica Acta* **68**(13): 2935-2946.
- 1188 Kleine, T., Mezger, K., Palme, H., and Münker, C., 2004b. The W isotope evolution of the
1189 bulk silicate Earth: constraints on the timing and mechanisms of core formation and
1190 accretion. *Earth and Planetary Science Letters* **228**(1-2): 109-123.
- 1191 Kleine, T., Münker, C., Mezger, K., and Palme, H., 2002. Rapid accretion and early core
1192 formation on asteroids and the terrestrial planets from Hf-W chronometry. *Nature*
1193 **418**(6901): 952-955.
- 1194 Kleine, T., Touboul, M., Bourdon, B., Nimmo, F., Mezger, K., Palme, H., Jacobsen, S.B.,
1195 Yin, Q.-Z., and Halliday, A.N., 2009. Hf-W chronology of the accretion and early
1196 evolution of asteroids and terrestrial planets. *Geochimica et Cosmochimica Acta*
1197 **73**(17): 5150-5188.
- 1198 Kleine, T., and Walker, R.J., 2017. Tungsten Isotopes in Planets. *Annual Review of Earth and*
1199 *Planetary Sciences* **45**(1): 389-417.
- 1200 König, S., Münker, C., Hohl, S., Paulick, H., Barth, A.R., Lagos, M., Pfander, J., and Büchl,
1201 A., 2011. The Earth's tungsten budget during mantle melting and crust formation.
1202 *Geochimica et Cosmochimica Acta* **75**(8): 2119-2136.
- 1203 Kruijer, T.S., and Kleine, T., 2017. Tungsten isotopes and the origin of the Moon. *Earth and*
1204 *Planetary Science Letters* **475**(Supplement C): 15-24.
- 1205 Kruijer, T.S., Kleine, T., Borg, L.E., Brennecke, G.A., Irving, A.J., Bischoff, A., and Agee,
1206 C.B., 2017. The early differentiation of Mars inferred from Hf-W chronometry. *Earth*
1207 *and Planetary Science Letters* **474**(Supplement C): 345-354.
- 1208 Kruijer, T.S., Kleine, T., Fischer-Gödde, M., and Sprung, P., 2015. Lunar tungsten isotopic
1209 evidence for the late veneer. *Nature* **520**(7548): 534-537.
- 1210 Lofgren, G.E., 1983. Effect of Heterogeneous Nucleation on Basaltic Textures: A Dynamic
1211 Crystallization Study. *Journal of Petrology* **24**(3): 229-255.
- 1212 Lorand, J.-P., and Alard, O., 2001. Platinum-group element abundances in the upper mantle:
1213 new constraints from in situ and whole-rock analyses of Massif Central xenoliths
1214 (France). *Geochimica et Cosmochimica Acta* **65**(16): 2789-2806.
- 1215 Ludwig, K.R. (2003). ISOPLOT 3.00. A geochronological toolkit for Microsoft Excel.
1216 Berkeley Geochronology Center Spec. Publ. No. 4: 70 pp.
- 1217 Luguet, A., Shirey, S.B., Lorand, J.-P., Horan, M.F., and Carlson, R.W., 2007. Residual
1218 platinum-group minerals from highly depleted harzburgites of the Lherz massif
1219 (France) and their role in HSE fractionation of the mantle. *Geochimica et*
1220 *Cosmochimica Acta* **71**(12): 3082-3097.
- 1221 Maier, W.D., Barnes, S.J., Campbell, I.H., Fiorentini, M.L., Peltonen, P., Barnes, S.J., and
1222 Smithies, R.H., 2009. Progressive mixing of meteoritic veneer into the early Earth's
1223 deep mantle. *Nature* **460**(7255): 620-623.
- 1224 Mavrogenes, J.A., and O'Neill, H.S.C., 1999. The relative effects of pressure, temperature and
1225 oxygen fugacity on the solubility of sulfide in mafic magmas. *Geochimica et*
1226 *Cosmochimica Acta* **63**(7-8): 1173-1180.

- 1227 McDonough, W.F. (2004). Compositional model for the Earth's core. Treatise on
1228 Geochemistry. Amsterdam, Elsevier. **2**: 547-568.
- 1229 Meisel, T., and Moser, J., 2004. Platinum-group element and rhenium concentrations in low-
1230 abundance reference materials. GEOSTANDARDS AND GEOANALYTICAL
1231 RESEARCH **28**(2): 233-250.
- 1232 Meisel, T., Walker, R.J., Irving, A.J., and Lorand, J.-P., 2001. Osmium isotopic compositions
1233 of mantle xenoliths: A global perspective. *Geochimica et Cosmochimica Acta* **65**(8):
1234 1311-1323.
- 1235 Mertzman, S.A., 2000. K-Ar results from the southern Oregon - northern California Cascade
1236 range. *Oregon Geology* **62**(4): 99-122.
- 1237 Morgan, J.W., 1985. Osmium isotope constraints on Earth's late accretionary history. *Nature*
1238 **317**(6039): 703-705.
- 1239 Morgan, J.W., Ganapathy, R., Higuchi, H., and Anders, E. (1977). Meteoritic Material on the
1240 Moon. The Soviet-American Conference on Cosmochemistry of the Moon,
1241 Washington, DC, NASA SP-370, US Govt. Printing Office.
- 1242 Morgan, J.W., Wanderless, G.A., Petrie, R.K., and Irving, A.J., 1981. Composition of the
1243 earth's upper mantle, I. Siderophile trace elements in ultramafic nodules.
1244 *Tectonophysics* **75**(1-2): 47-67.
- 1245 Mundl, A., Touboul, M., Jackson, M.G., Day, J.M.D., Kurz, M.D., Lekic, V., Helz, R.T., and
1246 Walker, R.J., 2017. Tungsten-182 heterogeneity in modern ocean island basalts.
1247 *Science* **356**(6333): 66-69.
- 1248 Nesbitt, R.W., Sun, S.S., and Purvis, A.C., 1979. Komatiites: geochemistry and genesis.
1249 *Canadian Mineralogist* **17**(2): 165-186.
- 1250 Norman, M.D., 2005. Lunar impact breccias: Petrology, crater setting, and bombardment
1251 history of the Moon. *Australian Journal of Earth Sciences* **52**(4-5): 711-723.
- 1252 Norman, M.D., Bennett, V.C., and Ryder, G., 2002. Targeting the impactors: siderophile
1253 element signatures of lunar impact melts from Serenitatis. *Earth and Planetary Science
1254 Letters* **202**(2): 217-228.
- 1255 O'Neil, J., Carlson, R.W., Francis, D., and Stevenson, R.K., 2008. Neodymium-142 evidence
1256 for Hadean mafic crust. *Science* **321**(5897): 1828-1831.
- 1257 O'Neil, J., Carlson, R.W., Paquette, J.-L., and Francis, D., 2012. Formation age and
1258 metamorphic history of the Nuvvuagittuq Greenstone Belt. *Precambrian Research*
1259 **220-221**: 23-44.
- 1260 O'Neil, J., Rizo, H., Boyet, M., Carlson, R.W., and Rosing, M.T., 2016. Geochemistry and Nd
1261 isotopic characteristics of Earth's Hadean mantle and primitive crust. *Earth and
1262 Planetary Science Letters* **442**: 194-205.
- 1263 O'Neill, C., and Debaille, V., 2014. The evolution of Hadean-Eoarchean geodynamics. *Earth
1264 and Planetary Science Letters* **406**: 49-58.
- 1265 Ohtani, E., 1984. Generation of komatiite magma and gravitational differentiation in the deep
1266 upper mantle. *Earth and Planetary Science Letters* **67**(2): 261-272.
- 1267 Ohtani, E., 1990. Majorite fractionation and genesis of komatiites in the deep mantle.
1268 *Precambrian Research* **48**(3): 195-202.
- 1269 Puchtel, I.S., Blichert-Toft, J., Touboul, M., Horan, M.F., and Walker, R.J., 2016a. The
1270 coupled ^{182}W - ^{142}Nd record of early terrestrial mantle differentiation. *Geochemistry,
1271 Geophysics, Geosystems* **17**(6): 2168-2193.
- 1272 Puchtel, I.S., Blichert-Toft, J., Touboul, M., Walker, R.J., Byerly, G., Nisbet, E.G., and
1273 Anhaeusser, C.R., 2013. Insights into early Earth from Barberton komatiites: Evidence
1274 from lithophile isotope and trace element systematics. *Geochimica et Cosmochimica
1275 Acta* **108**: 63-90.

- 1276 Puchtel, I.S., Brandon, A.D., and Humayun, M., 2004a. Precise Pt-Re-Os isotope systematics
1277 of the mantle from 2.7-Ga komatiites. *Earth and Planetary Science Letters* **224**(1-2):
1278 157-174.
- 1279 Puchtel, I.S., Brandon, A.D., Humayun, M., and Walker, R.J., 2005. Evidence for the early
1280 differentiation of the core from Pt-Re-Os isotope systematics of 2.8-Ga komatiites.
1281 *Earth and Planetary Science Letters* **237**(1-2): 118-134.
- 1282 Puchtel, I.S., and Humayun, M., 2005. Highly siderophile element geochemistry of ^{187}Os -
1283 enriched 2.8-Ga Kostomuksha komatiites, Baltic Shield. *Geochimica et
1284 Cosmochimica Acta* **69**(6): 1607-1618.
- 1285 Puchtel, I.S., Humayun, M., Campbell, A., Sproule, R., and Lesher, C.M., 2004b. Platinum
1286 group element geochemistry of komatiites from the Alexo and Pyke Hill areas,
1287 Ontario, Canada. *Geochimica et Cosmochimica Acta* **68**(6): 1361-1383.
- 1288 Puchtel, I.S., Humayun, M., and Walker, R.J., 2007. Os-Pb-Nd isotope and highly siderophile
1289 and lithophile trace element systematics of komatiitic rocks from the Volotsk suite, SE
1290 Baltic Shield. *Precambrian Research* **158**(1-2): 119-137.
- 1291 Puchtel, I.S., Touboul, M., Blichert-Toft, J., Walker, R.J., Brandon, A.D., Nicklas, R.W.,
1292 Kulikov, V.S., and Samsonov, A.V., 2016b. Lithophile and siderophile element
1293 systematics of the mantle at the Archean-Proterozoic boundary: Evidence from 2.4 Ga
1294 komatiites. *Geochimica et Cosmochimica Acta* **180**: 227-255.
- 1295 Puchtel, I.S., Walker, R.J., Anhaeusser, C.R., and Gruau, G., 2009a. Re-Os isotope
1296 systematics and HSE abundances of the 3.5 Ga Schapenburg komatiites, South Africa:
1297 Hydrous melting or prolonged survival of primordial heterogeneities in the mantle?
1298 *Chemical Geology* **262**(3-4): 355-369.
- 1299 Puchtel, I.S., Walker, R.J., Brandon, A.D., and Nisbet, E.G., 2009b. Pt-Re-Os and Sm-Nd
1300 isotope and HSE and REE systematics of the 2.7 Ga Belingwe and Abitibi komatiites.
1301 *Geochimica et Cosmochimica Acta* **73**(20): 6367-6389.
- 1302 Puchtel, I.S., Walker, R.J., James, O.B., and Krueger, D.A., 2008. Osmium isotope and highly
1303 siderophile element systematics of lunar impact melt breccias: Implications for the late
1304 accretion history of the Moon and Earth. *Geochimica et Cosmochimica Acta* **72**(12):
1305 3022-3042.
- 1306 Puchtel, I.S., Walker, R.J., Touboul, M., Nisbet, E.G., and Byerly, G.R., 2014. Insights into
1307 Early Earth from the Pt-Re-Os isotope and Highly Siderophile Element abundance
1308 systematics of Barberton komatiites. *Geochimica et Cosmochimica Acta* **125**: 394-
1309 413.
- 1310 Rehkämper, M., and Halliday, A.N., 1997. Development and application of new ion-exchange
1311 techniques for the separation of the platinum-group and other siderophile elements
1312 from geological samples. *Talanta* **44**(4): 663-672.
- 1313 Righter, K., Walker, R.J., and Warren, P.H. (2000). Significance of highly siderophile
1314 elements and osmium isotopes in the lunar and terrestrial mantles. *Origin of the Earth
1315 and Moon*. Righter, K. and Canup, R.M. Tucson, University of Arizona Press: 291-
1316 322.
- 1317 Ringwood, A.E., 1992. Volatile and siderophile element geochemistry of the Moon: a
1318 reappraisal. *Earth and Planetary Science Letters* **111**(2): 537-555.
- 1319 Rizo, H., Boyet, M., Blichert-Toft, J., O'Neil, J., Rosing, M.T., and Paquette, J.-L., 2012. The
1320 elusive Hadean enriched reservoir revealed by ^{142}Nd deficits in Isua Archaean rocks.
1321 *Nature* **491**(7422): 96-100.
- 1322 Rizo, H., Boyet, M., Blichert-Toft, J., and Rosing, M., 2011. Combined Nd and Hf isotope
1323 evidence for deep-seated source of Isua lavas. *Earth and Planetary Science Letters*
1324 **312**(3-4): 267-279.

- 1325 Rizo, H., Boyet, M., Blichert-Toft, J., and Rosing, M.T., 2013. Early mantle dynamics
 1326 inferred from ^{142}Nd variations in Archean rocks from southwest Greenland. *Earth and*
 1327 *Planetary Science Letters* **377-378**: 324-335.
- 1328 Rizo, H., Walker, R.J., Carlson, R.W., Horan, M.F., Mukhopadhyay, S., Manthos, V., Francis,
 1329 D., and Jackson, M.G., 2016a. Preservation of Earth-forming events in the tungsten
 1330 isotopic composition of modern flood basalts. *Science* **352**(6287): 809-812.
- 1331 Rizo, H., Walker, R.J., Carlson, R.W., Touboul, M., Horan, M.F., Puchtel, I.S., Boyet, M.,
 1332 and Rosing, M.T., 2016b. Early Earth differentiation investigated through ^{142}Nd , ^{182}W ,
 1333 and highly siderophile element abundances in samples from Isua, Greenland.
 1334 *Geochimica et Cosmochimica Acta* **175**: 319-336.
- 1335 Roth, A.S.G., Bourdon, B., Mojzsis, S.J., Touboul, M., Sprung, P., Guitreau, M., and
 1336 Blichert-Toft, J., 2013. Inherited ^{142}Nd anomalies in Eoarchean protoliths. *Earth and*
 1337 *Planetary Science Letters* **361**: 50-57.
- 1338 Rubie, D.C., Melosh, H.J., Reid, J.E., Liebske, C., and Righter, K., 2003. Mechanisms of
 1339 metal-silicate equilibration in the terrestrial magma ocean. *Earth and Planetary*
 1340 *Science Letters* **205**(3-4): 239-255.
- 1341 Scherer, E., Münker, C., and Mezger, K., 2001. Calibration of the lutetium-hafnium clock.
 1342 *Science* **293**(5530): 683-687.
- 1343 Schoenberg, R., Kamber, B.S., Collerson, K.D., and Eugster, O., 2002. New W-isotope
 1344 evidence for rapid terrestrial accretion and very early core formation. *Geochimica et*
 1345 *Cosmochimica Acta* **66**(17): 3151-3160.
- 1346 Schulz, K.J. (1982). Magnesian basalts from the Archean terrains of Minnesota. *Komatiites*.
 1347 Arndt, N.T. and Nisbet, E.G. London, George Allen and Unwin: 171-186.
- 1348 Shirey, S.B., and Walker, R.J., 1998. The Re-Os isotope system in cosmochemistry and high-
 1349 temperature geochemistry. *Annual Reviews of Earth and Planetary Sciences* **26**: 423-
 1350 500.
- 1351 Smoliar, M.I., Walker, R.J., and Morgan, J.W., 1996. Re-Os ages of Group IIA, IIIA, IVA,
 1352 and IVB iron meteorites. *Science* **271**(5762): 1099-1102.
- 1353 Söderlund, U., Patchett, J.P., Vervoort, J.D., and Isachsen, C.E., 2004. The ^{176}Lu decay
 1354 constant determined by Lu-Hf and U-Pb isotope systematics of Precambrian mafic
 1355 intrusions. *Earth and Planetary Science Letters* **219**(3-4): 311-324.
- 1356 Stone, W.E., Crocket, J.H., Dickin, A.P., and Fleet, M.E., 1995a. Origin of Archean
 1357 ferropicrites: geochemical constraints from the Boston Creek Flow, Abitibi greenstone
 1358 belt, Ontario, Canada. *Chemical Geology* **121**(1-4): 51-71.
- 1359 Stone, W.E., Crocket, J.H., and Fleet, M.E., 1995b. Differentiation processes in an unusual
 1360 iron-rich alumina-poor Archean ultramafic/mafic igneous body, Ontario.
 1361 *Contributions to Mineralogy and Petrology* **119**(2-3): 287-300.
- 1362 Stone, W.E., Jensen, L.S., and Church, W.R., 1987. Petrography and geochemistry of an
 1363 unusual Fe-rich basaltic komatiite from Boston Township, Northeastern Ontario.
 1364 *Canadian Journal of Earth Sciences* **24**(12): 2537-2550.
- 1365 Tomlinson, K.Y., Hughes, D.J., Thurston, P.C., and Hall, R.P., 1999. Plume magmatism and
 1366 crustal growth at 2.9 to 3.0 Ga in the Steep Rock and Lumby Lake area, Western
 1367 Superior Province. *Lithos* **46**(1): 103-136.
- 1368 Touboul, M., Kleine, T., Bourdon, B., Palme, H., and Wieler, R., 2007. Late formation and
 1369 prolonged differentiation of the Moon inferred from W isotopes in lunar metals.
 1370 *Nature* **450**(7173): 1206-1209.
- 1371 Touboul, M., Liu, J., O'Neil, J., Puchtel, I.S., and Walker, R.J., 2014. New Insights into the
 1372 Hadean Mantle Revealed by ^{182}W and Highly Siderophile Element Abundances of
 1373 Supracrustal Rocks from the Nuvvuagittuq Greenstone Belt, Quebec, Canada.
 1374 *Chemical Geology*(383): 63-75.

- 1375 Touboul, M., Puchtel, I.S., and Walker, R.J., 2012. ^{182}W Evidence for Long-Term
1376 Preservation of Early Mantle Differentiation Products. *Science* **335**: 1065-1069.
- 1377 Touboul, M., Puchtel, I.S., and Walker, R.J., 2015. Tungsten isotopic evidence for
1378 disproportional late accretion to the Earth and Moon. *Nature* **520**(7548): 530-533.
- 1379 Touboul, M., and Walker, R.J., 2012. High precision tungsten isotope measurement by
1380 thermal ionization mass spectrometry. *INTERNATIONAL JOURNAL OF MASS
1381 SPECTROMETRY* **309**: 109-117.
- 1382 Walker, R.J., 2009. Highly siderophile elements in the Earth, Moon and Mars: Update and
1383 implications for planetary accretion and differentiation. *Chemie der Erde -
1384 Geochemistry* **69**(2): 101-125.
- 1385 Walker, R.J., 2014. Siderophile element constraints on the origin of the Moon.
1386 *PHILOSOPHICAL TRANSACTIONS OF THE ROYAL SOCIETY OF LONDON
1387 372*: 20130258.
- 1388 Walker, R.J., Horan, M.F., Morgan, J.W., Becker, H., Grossman, J.N., and Rubin, A.E., 2002.
1389 Comparative ^{187}Re - ^{187}Os systematics of chondrites: Implications regarding early solar
1390 system processes. *Geochimica et Cosmochimica Acta* **66**(23): 4187-4201.
- 1391 Walker, R.J., Horan, M.F., Shearer, C.K., and Papike, J.J., 2004. Low abundances of highly
1392 siderophile elements in the lunar mantle: Evidence for prolonged late accretion. *Earth
1393 and Planetary Science Letters* **224**(3-4): 399-413.
- 1394 Walker, R.J., and Stone, W.E., 2001. Os isotope constraints on the origin of the 2.7 Ga Boston
1395 Creek Flow, Ontario, Canada. *Chemical Geology* **175**(3-4): 567-579.
- 1396 Warren, P.H. (2003). *The Moon. Treatise on Geochemistry*. Amsterdam, Elsevier. **1**: 559-
1397 599.
- 1398 Warren, P.H., Jerde, E.A., and Kallemeijn, G.W., 1989. Lunar meteorites: siderophile element
1399 contents, and implications for the composition and origin of the Moon. *Earth and
1400 Planetary Science Letters* **91**(3): 245-260.
- 1401 Willbold, M., Elliott, T., and Moorbath, S., 2011. The tungsten isotopic composition of the
1402 Earth's mantle before the terminal bombardment. *Nature* **477**(7363): 195-198.
- 1403 Willbold, M., Mojzsis, S.J., Chen, H.W., and Elliott, T., 2015. Tungsten isotope composition
1404 of the Acasta Gneiss Complex. *Earth and Planetary Science Letters* **419**: 168-177.
- 1405 Yin, Q., Jacobsen, S.B., Yamashita, K., Blichert-Toft, J., Telouk, P., and Albarede, F., 2002.
1406 A short timescale for terrestrial planet formation from Hf-W chronometry of
1407 meteorites. *Nature* **418**(6901): 949-952.
- 1408
1409

1410 **Figure captions**

1411 **Fig. 1.** Integrated schematic section of the Boston Creek Flow (BCF) sampled in this study.
1412 Samples J17 and 2-18 are from the Walker and Stone (2001) study. Shown are textural
1413 variations within the BCF, sample numbers, their location in the sequence, and MgO
1414 contents (wt. %).

1415 **Fig. 2.** Abundances of selected major (wt. %) and lithophile trace (ppm) elements and W
1416 (ppb) obtained in this study plotted against MgO contents (wt. %) in the BCF. Highlighted
1417 in the W versus MgO diagram are the two sample powders from the Walker and Stone
1418 (2001) study analyzed here, which likely experienced W contamination during sample
1419 preparation. See text for additional details.

1420 **Fig. 3. a.** BSE-normalized abundances of lithophile trace elements in the BCF arranged in
1421 decreasing order of incompatibility during mantle melting. The normalizing values for W
1422 are from (Arevalo and McDonough, 2008) and for the rest of the elements from
1423 (Hofmann, 1988); **b, c.** Diagrams of W/W* and $\mu^{182}\text{W}$ versus LOI (loss on ignition) for
1424 the BCF. Highlighted are two samples from the Walker and Stone (2001) study analyzed
1425 here, which likely experienced W contamination during sample preparation. Note the
1426 positive correlation between the index of alteration (LOI) and the magnitude of the W
1427 abundance anomaly likely indicating post-magmatic control on the W abundance
1428 variations in the BCF, and the lack thereof between the index of alteration and the
1429 magnitude of the positive ^{182}W anomaly likely indicating derivation of W from the BCF
1430 itself. See text for additional details.

1431 **Fig. 4.** Re-Os isochron diagram for samples from the BCF analyzed in this study. Sample
1432 BC06 plots well above the regression line and was excluded from the ISOPLOT
1433 regression calculations. See text for additional details.

1434 **Fig. 5.** CI chondrite-normalized HSE abundances in whole-rock samples from the BCF.
1435 Normalizing values are from (Horan *et al.*, 2003).

1436 **Fig. 6.** Abundances of the highly siderophile elements in the BCF (ppb) obtained in this study
1437 plotted against MgO contents (wt. %).

1438 **Fig. 7.** Tungsten isotopic compositions of samples from the BCF analyzed in this study. The
1439 data are reported in $\mu^{182}\text{W}$ units, which are part per million (ppm) deviations of the
1440 $^{182}\text{W}/^{184}\text{W}$ ratio of a given sample relative to the mean $^{182}\text{W}/^{184}\text{W}$ ratio measured for the
1441 Alfa Aesar W standard. Each symbol corresponds to a separately digested sample.

1442 **Fig. 8.** Neodymium isotopic compositions of samples from the BCF analyzed in this study.
1443 The data are reported in $\mu^{142}\text{Nd}$ units, which are part per million (ppm) deviations of the
1444 $^{142}\text{Nd}/^{144}\text{Nd}$ ratio of a given sample relative to the mean $^{142}\text{Nd}/^{144}\text{Nd}$ ratio measured for
1445 the Nd standard AMES with an external precision of 2.8 ppm over the two-year period
1446 leading up to the present analytical campaign. Each symbol corresponds to a separately
1447 digested sample. Data for three separate digestions of the USGS GRM BCR-1 are
1448 reported for reference.

1449 **Fig. 9. (a)** $^{147}\text{Sm}-^{143}\text{Nd}$ and **(b)** $^{176}\text{Lu}-^{176}\text{Hf}$ isochron diagrams for samples from the BCF
1450 analyzed in this study. See text for additional details. **(c)** Diagram illustrating the initial
1451 $\epsilon^{143}\text{Nd}$ and $\epsilon^{176}\text{Hf}$ values for the mantle source of the BCF and for the Chondritic Uniform
1452 Reservoir (CHUR) and Depleted MORB Mantle (DMM) calculated at the time of BCF

1453 emplacement (2720 Ma). The CHUR and DMM parameters are from (Jacobsen and
1454 Wasserburg, 1980), (Bouvier *et al.*, 2008), and (Blichert-Toft and Puchtel, 2010). Note the
1455 coupled, or congruent, behavior between the two isotope systems in the source of the BCF
1456 resulting in the data plotting on the terrestrial array.

1457 **Fig. 10.** Initial $^{187}\text{Os}/^{188}\text{Os}$ isotopic compositions, expressed in $\gamma^{187}\text{Os}$ terms, of the Archean
1458 komatiite systems plotted as a function of age. The data are from (Foster *et al.*, 1996;
1459 Puchtel *et al.*, 2004a; Puchtel *et al.*, 2005; Puchtel *et al.*, 2007; Puchtel *et al.*, 2009a;
1460 Puchtel *et al.*, 2009b; Puchtel *et al.*, 2014; Puchtel *et al.*, 2016a; Puchtel *et al.*, 2016b) and
1461 this study. The data for chondritic meteorites are compiled from (Walker *et al.*, 2002;
1462 Brandon *et al.*, 2005; Fischer-Gödde *et al.*, 2010).

1463 **Fig. 11.** Calculated total Pt and Pd abundances in the sources of Archean komatiite systems
1464 plotted as *per cent* of the total Pt and Pd abundances in the estimates for modern BSE of
1465 (Becker *et al.*, 2006). The sources of the data are as follows. 2.41 Ga Vredefort Belt -
1466 (Puchtel *et al.*, 2016b); 2.69 Ga Belingwe - (Puchtel *et al.*, 2009b); 2.72 Ga Pyke Hill and
1467 Alexo - (Puchtel *et al.*, 2004b); 2.72 Ga Boston Creek - this study; 2.82 Ga Kostomuksha
1468 - (Puchtel and Humayun, 2005); 2.88 Ga Volotsk-Kamennozero - (Puchtel *et al.*, 2007);
1469 3.26 Ga Weltevreden and 3.48 Ga Komati - (Puchtel *et al.*, 2014); 3.55 Ga Schapenburg -
1470 (Puchtel *et al.*, 2016a). Uncertainties are 2SD. See text for additional details.

1471 **Fig. 12.** $\mu^{182}\text{W}$ versus total calculated HSE abundances in the sources of Archean komatiite
1472 systems studied to-date relative to those in the estimates for the present-day BSE of
1473 (Becker *et al.*, 2006). This proportion corresponds to the fraction of the total HSE budget
1474 of the BSE added during late accretion assuming an HSE-free Earth mantle prior to late
1475 accretion. The $\mu^{182}\text{W}$ of the BSE prior to late accretion is constrained via ISOPLOT
1476 regression analysis of the $\mu^{182}\text{W}$ and HSE compositions of the BCF and the present-day
1477 BSE to be $+18 \pm 7$ ppm. The $\mu^{182}\text{W}$ for the lunar mantle of $+25 \pm 5$ ppm (Kruijer *et al.*,
1478 2015; Touboul *et al.*, 2015) is identical to the estimate for the pre-late accretion Earth
1479 mantle, thus, providing further support to the notion that the Moon and Earth formed from
1480 material with identical ^{182}W compositions (Kleine and Walker, 2017). The W isotopic
1481 data and estimates of the total HSE contents for the komatiite systems are from (Puchtel
1482 and Humayun, 2005; Touboul *et al.*, 2012; Puchtel *et al.*, 2014; Puchtel *et al.*, 2016a;
1483 Puchtel *et al.*, 2016b), and this study.

1485

Table 1. Major (wt. %) and minor (ppm) element data for the USGS GRM BIR-1, BCR-1, and BHVO-2

Sample	BIR-1_1	BIR-1_2	BIR-1_3	BIR-1_4	BIR-1_5	Average ($\pm 2\text{SD}$)	GeOReM ($\pm 2\text{SE}$)	BCR-1	GeOReM ($\pm 2\text{SE}$)	BHVO-2	GeOReM ($\pm 2\text{SE}$)
SiO₂	47.1	47.2	47.2	46.8	47.0	47.1 \pm 0.4	47.8 \pm 0.2	53.9	54.5 \pm 0.5	48.9	49.6 \pm 0.1
TiO₂	0.946	0.939	0.945	0.947	0.965	0.948 \pm 0.020	0.959 \pm 0.007	2.28	2.24 \pm 0.04	2.69	2.73 \pm 0.02
Al₂O₃	15.5	15.5	15.6	15.3	15.3	15.5 \pm 0.2	15.5 \pm 0.1	13.8	13.6 \pm 0.1	13.5	13.4 \pm 0.1
Fe₂O₃	11.2	11.5	11.5	11.5	11.4	11.4 \pm 0.2	11.4 \pm 0.1	13.6	13.4 \pm 0.2	12.6	12.4 \pm 0.1
MnO	0.180	0.170	0.157	0.172	0.190	0.174 \pm 0.025	0.173 \pm 0.002	0.201	0.183 \pm 0.003	0.150	0.169 \pm 0.002
MgO	9.70	9.57	9.86	9.71	9.69	9.71 \pm 0.20	9.69 \pm 0.05	3.69	3.47 \pm 0.04	7.44	7.26 \pm 0.04
CaO	13.3	13.1	13.4	13.3	13.2	13.3 \pm 0.2	13.3 \pm 0.1	7.17	7.12 \pm 0.22	11.5	11.4 \pm 0.1
Na₂O	1.78	1.79	1.85	1.91	1.80	1.83 \pm 0.11	1.83 \pm 0.02	3.22	3.33 \pm 0.05	2.20	2.22 \pm 0.05
K₂O	0.010	0.012	0.015	0.010	0.008	0.011 \pm 0.01	0.029 \pm 0.003	1.80	1.73 \pm 0.02	0.478	0.513 \pm 0.004
P₂O₅	0.025	0.028	0.021	0.019	0.016	0.022 \pm 0.010	0.030 \pm 0.004	0.36	0.36 \pm 0.01	0.253	0.269 \pm 0.005
Total	99.78	99.83	100.54	99.62	99.63	99.88	100.70	99.91	99.96	99.68	99.99
LOI	-0.35	-0.31	-0.33	-0.06	-0.48	-0.31		0.37		-0.33	
Cr	417	417	409	382	384	402 \pm 35	393 \pm 4	16	14 \pm 1	314	287 \pm 3
Ni	140	134	145	159	146	145 \pm 19	169 \pm 2	15	12 \pm 1	144	120 \pm 1

1486

1487

1488 **Table 2.** HSE abundances (in ppb) and Os isotopic data for the SRM MUH-1, OKUM, and TDB-1.

Sample	Re	Os	Ir	Ru	Pt	Pd	$^{187}\text{Os}/^{188}\text{Os}$
MUH-1	0.183	3.42	3.65	6.90	8.25	8.10	0.12728±6
OKUM	0.471	0.722	0.813	4.40	12.6	11.5	0.27781±14
TDB-1	0.788	0.109	0.0606	0.204	4.89	21.5	1.1543±9
MUH-1 reference	0.182	4.13	3.78	7.23	9.76	8.88	0.1280
2SD	0.047	2.95	1.22	0.87	3.01	1.36	0.0034
OKUM reference	0.499	0.847	1.00	4.66	11.8	11.5	0.2666
2SD	0.076	0.24	0.26	1.12	2.9	2.1	0.0090
TDB-1 reference¹	0.795	0.117	0.0744	0.198	5.01	24.4	0.916
2SD	0.045	0.022	0.0188	0.017	0.36	3.8	0.195
TDB-1 reference²	1.01	0.106	0.059	0.231	4.74	22.3	0.973
2SD	0.07	0.020	0.011	0.079	1.19	3.7	0.128

1489 The MUH-1 and OKUM reference values are from Burnham *et al.* (2010) and the TDB-1 reference values
1490 are from ¹(Meisel and Moser, 2004) and ²(Dale *et al.*, 2012).

1491

1492

1493

Table 3. Major (wt. %) and minor (ppm) element data for the Boston Creek Flow

Sample	BC01	BC02	BC03	BC06	BC07	BC08	BC09	BC10	J17_1	J17	2-18
SiO₂	44.6	46.8	47.4	44.7	40.6	38.4	40.8	39.6	40.9	40.7	41.5
TiO₂	1.376	1.335	1.368	1.238	0.628	0.415	0.632	0.486	0.480	0.470	0.531
Al₂O₃	7.89	7.65	8.00	6.98	3.06	2.04	3.07	2.34	2.38	2.36	2.76
Fe₂O₃	19.3	17.5	18.3	19.2	22.1	20.1	22.2	20.8	18.0	17.7	18.0
MnO	0.263	0.244	0.247	0.326	0.306	0.319	0.316	0.298	0.249	0.248	0.242
MgO	8.26	8.88	8.17	13.4	28.5	34.0	28.8	32.1	32.8	33.4	31.8
CaO	16.63	14.42	13.74	13.10	4.13	3.50	3.50	3.63	4.08	4.00	3.96
Na₂O	1.92	2.27	2.43	0.63	0.10	0.08	0.11	0.08	0.04	0.04	0.06
K₂O	0.216	0.162	0.190	0.136	0.009	0.006	0.006	0.000	0.000	0.000	0.001
P₂O₅	0.083	0.088	0.088	0.071	0.034	0.035	0.032	0.026	0.030	0.030	0.040
Total	100.53	99.38	99.85	99.79	99.52	98.91	99.38	99.40	98.90	98.96	98.96
LOI	5.82	2.99	1.57	3.61	6.73	11.31	6.56	7.89	8.58	8.47	8.29
Cr	559	586	440	746	2261	4443	2180	3685	4709	4669	3762
Ni	247	213	181	397	1914	3166	2062	2790	2922	2505	3449
Al₂O₃/TiO₂	5.7	5.7	5.8	5.6	4.9	4.9	4.9	4.8	5.0	5.0	5.2

1494

1495

1496

Note. Analyses were re-calculated on an anhydrous basis, but not re-normalized to 100% in order to preserve information on the quality of the analyses.

1497

1498

Table 4. Trace element data (ppm) for the Boston Creek Flow

Sample	BC01	BC02	BC03	BC06	BC07	BC08	Replicate	BC09	BC10	Replicate	J17_1	J17	2-18	Replicate
Th	0.936	0.936	0.940	0.851	0.384	0.273	0.268	0.372	0.295	0.283	0.304	0.315	0.344	0.340
U	0.263	0.264	0.259	0.231	0.115	0.0787	0.0747	0.106	0.0833	0.0782	0.0831	0.0873	0.0962	0.0980
Nb	11.1	10.4	10.4	9.35	4.46	3.32	3.38	4.17	3.37	3.40	3.88	3.92	4.09	4.08
La	11.7	11.8	12.1	9.87	4.69	3.16	3.22	4.46	3.59	3.60	3.76	3.54	3.89	3.70
Ce	28.5	27.7	27.6	24.3	12.9	7.78	7.86	12.71	9.07	8.90	9.09	9.19	10.9	10.5
Pr	3.96	4.06	4.12	3.32	1.66	1.14	1.11	1.66	1.17	1.16	1.38	1.42	1.66	1.59
Nd	16.9	17.3	17.5	14.3	7.03	4.75	4.65	6.91	5.56	5.49	5.88	5.90	6.34	6.24
Sm	3.77	3.87	3.88	3.30	1.54	1.02	1.00	1.51	1.24	1.19	1.26	1.27	1.41	1.37
Hf	2.00	1.99	1.96	1.74	0.766	0.527	0.477	0.836	0.647	0.620	0.575	0.556	0.664	0.650
Zr	67.2	63.7	64.7	59.9	27.1	17.6	16.9	27.2	19.3	20.8	20.4	19.7	21.4	21.4
Eu	1.26	1.22	1.26	1.05	0.449	0.333	0.321	0.405	0.349	0.339	0.394	0.408	0.407	0.412
Gd	3.82	3.90	4.01	3.44	1.57	1.00	0.957	1.53	1.14	1.11	1.23	1.23	1.38	1.38
Tb	0.553	0.564	0.567	0.517	0.230	0.142	0.136	0.222	0.165	0.158	0.172	0.172	0.200	0.202
Dy	3.35	3.32	3.35	3.11	1.35	0.830	0.806	1.35	0.975	0.947	1.01	1.02	1.17	1.19
Y	15.8	15.5	16.1	14.8	6.25	3.87	3.64	6.43	4.72	4.45	4.51	4.58	5.17	5.07
Ho	0.642	0.646	0.655	0.608	0.263	0.162	0.155	0.262	0.192	0.184	0.192	0.193	0.222	0.224
Er	1.76	1.78	1.79	1.67	0.725	0.442	0.423	0.722	0.535	0.508	0.515	0.514	0.605	0.598
Tm	0.248	0.244	0.254	0.230	0.104	0.0623	0.0594	0.102	0.0725	0.0693	0.0701	0.0711	0.0829	0.0826
Yb	1.55	1.57	1.63	1.49	0.661	0.398	0.384	0.651	0.468	0.445	0.451	0.457	0.531	0.532
Lu	0.227	0.225	0.231	0.2159	0.0944	0.0585	0.0569	0.0951	0.0659	0.0638	0.0650	0.0662	0.0779	0.0788
Ti/Zr	123	126	127	124	139	142	147	139	151	140	141	143	149	149
Nb/Nb*	1.21	1.14	1.12	1.17	1.20	1.29	1.32	1.17	1.18	1.22	1.31	1.34	1.28	1.32
(La/Sm) _N	1.95	1.92	1.95	1.88	1.92	1.96	2.02	1.86	1.82	1.90	1.87	1.76	1.74	1.70
(Gd/Yb) _N	1.99	2.01	1.99	1.87	1.92	2.02	2.01	1.90	1.98	2.02	2.20	2.16	2.09	2.10

1499

1500

1501

Note. Analyses were recalculated on an anhydrous basis.

N- normalized to the BSE values of (Hofmann, 1988).

1502

Table 5. HSE abundances (ppb), Re-Os isotopic data, and elemental ratios for the Boston Creek Flow

Sample	Re	Os	Ir	Ru	Pt	Pd	$^{187}\text{Re}/^{188}\text{Os}$	$^{187}\text{Os}/^{188}\text{Os}$	$\gamma^{187}\text{Os}(T)$	$(\text{Os/Ir})_N$	$(\text{Ru/Ir})_N$	$(\text{Pd/Ir})_N$
BC02	1.061	0.08087	0.201	0.838	6.94	8.37	101.7 ± 0.9	4.8334 ± 50	+7.8	0.390	2.85	32.6
BC03	0.1678	0.04221	0.188	0.576	7.09	8.50	21.61 ± 0.25	1.1180 ± 6	+7.3	0.217	2.09	35.3
BC06	0.5516	0.07389	0.185	0.825	6.16	7.44	47.82 ± 0.37	2.6668 ± 11	+315	0.386	3.04	31.3
BC08	0.04416	0.3792	0.397	5.52	2.97	2.84	0.5619 ± 0.0034	0.13798 ± 6	+3.3	0.926	9.50	5.60
BC08 replicate	0.04436	0.3687	0.395	5.51	2.99	2.77	0.5806 ± 0.0035	0.13860 ± 8	+3.0	0.906	9.54	5.48
BC09	0.1193	0.1644	0.338	4.46	3.91	4.34	3.573 ± 0.024	0.29284 ± 17	+17	0.472	9.01	10.0
BC10	0.1127	0.3958	0.780	7.46	3.05	3.51	1.382 ± 0.008	0.18112 ± 8	+8.0	0.492	6.54	3.51
BC10 replicate	0.1138	0.3979	0.749	7.39	3.02	3.16	1.388 ± 0.008	0.18199 ± 13	+8.5	0.515	6.74	3.30
J17_1	0.04875	2.354	1.94	6.94	3.25	3.26	0.0996 ± 0.0006	0.11356 ± 5	+0.52	1.18	2.45	1.32
J17_1 replicate	0.04803	2.321	1.88	6.45	3.38	3.29	0.0995 ± 0.0006	0.11352 ± 6	+0.48	1.20	2.34	1.37
J17	0.07042	2.233	1.82	6.76	3.25	3.27	0.1517 ± 0.0009	0.11334 ± 4	-1.9	1.19	2.54	1.40
<i>Corrected*</i>	0.04421	2.233					0.1033 ± 0.0006	0.11334 ± 4	+0.15			
J17 replicate	0.07155	2.367	1.89	6.50	3.34	3.25	0.1454 ± 0.0009	0.11305 ± 5	-1.9	1.21	2.35	1.34
<i>Corrected*</i>	0.04492	2.367					0.0990 ± 0.0006	0.11305 ± 5	+0.07			
2-18	0.08796	2.973	2.47	6.26	3.23	3.67	0.1423 ± 0.0009	0.11450 ± 3	-0.44	1.17	1.74	1.16
2-18 replicate	0.08643	2.946	2.38	5.63	3.31	3.66	0.1411 ± 0.0008	0.11450 ± 5	-0.39	1.20	1.61	1.20
J17**	0.09310	2.245					0.200 ± 0.005	0.11418 ± 5	-3.2			
J17** replicate	0.09495	2.076					0.217 ± 0.005	0.11420 ± 5	-3.9			
2-18**	0.1379	2.924					0.227 ± 0.007	0.11509 ± 5	-3.5			

1503

1504

1505

1506

1507

1508

1509

1510

Note. The HSE abundances were re-calculated on an anhydrous basis. The initial $\gamma^{187}\text{Os}$ values were calculated for $T = 2720$ Ma using the parameters specified in the text. Sample **BC06** plots well above the isochron and was not included in the regression calculations. The HSE normalizing values are from (Horan *et al.*, 2003). *Re abundance corrected for estimated 46% Re contamination during sample preparation in the (Walker and Stone, 2001) study. **Data from the Walker and Stone (2001) study. Samples **J17** and **2-18** are the same sample powders analyzed here and by Walker and Stone (2001), whereas sample **J17_1** is a new powder prepared in this study using uncrushed sample **J17** from the Walker and Stone (2001) study and metal-free equipment. Note the ~50% higher Re abundances obtained for the sample powder **J17** by Walker and Stone (2001) compared to this study, and also ~46% higher Re abundances in the sample powder **J17** relative to **J17_1** obtained in this study.

1511 **Table 6.** Tungsten abundances (in ppb) and W isotopic compositions
 1512 of the Boston Creek Flow

Sample	W ($\pm 2\text{SE}$)	$\mu^{182}\text{W} (\pm 2\text{SE})$
BC01	385 \pm 4	+7.6 \pm 2.1
Replicate	392 \pm 5	+7.4 \pm 4.8
BC02	346 \pm 3	+18.5 \pm 3.2
Replicate	344 \pm 5	+15.2 \pm 2.4
BC03	249 \pm 3	+14.6 \pm 3.4
Replicate	245 \pm 4	
BC06	469 \pm 5	+11.2 \pm 3.1
Replicate	485 \pm 6	
BC07	626 \pm 6	+11.2 \pm 6.4
Replicate	618 \pm 7	+13.6 \pm 3.1
BC08	462 \pm 4	+10.6 \pm 2.7
Replicate	458 \pm 6	
BC09	811 \pm 8	+9.3 \pm 2.1
Replicate	815 \pm 9	+7.2 \pm 3.1
BC10	319 \pm 3	+13.9 \pm 3.3
Replicate	313 \pm 5	
J17_1	347 \pm 5	
J17	1305 \pm 13	
2-18	675 \pm 7	

1513
 1514 **Note.** Abundances were re-calculated on an anhydrous basis. Uncertainties on W isotopic
 1515 compositions for individual samples are the 2SE in-run statistics of the individual analyses.
 1516 Samples **J17** and **2-18** are the powders from the Walker and Stone (2001) study, whereas
 1517 sample **J17_1** is the new powder prepared in this study using un-crushed material for sample
 1518 **J17** and metal-free equipment. Note $\sim 4\times$ higher W abundances in **J17** compared to **J17_1**
 1519 likely due to W contamination of the sample during processing in metal in the Walker and
 1520 Stone (2001) study, also consistent with $\sim 50\%$ higher Re abundance in that powder. Sample
 1521 **2-18**, which has $\sim 2\times$ higher W abundances than **J17_1**, is also likely contaminated with W
 1522 (and probably Re) during processing in metal in the Walker and Stone (2001) study.
 1523

1524 **Table 7.** Sm-Nd isotope and concentration data for the Boston Creek Flow and the USGS
 1525 GRM BCR-1

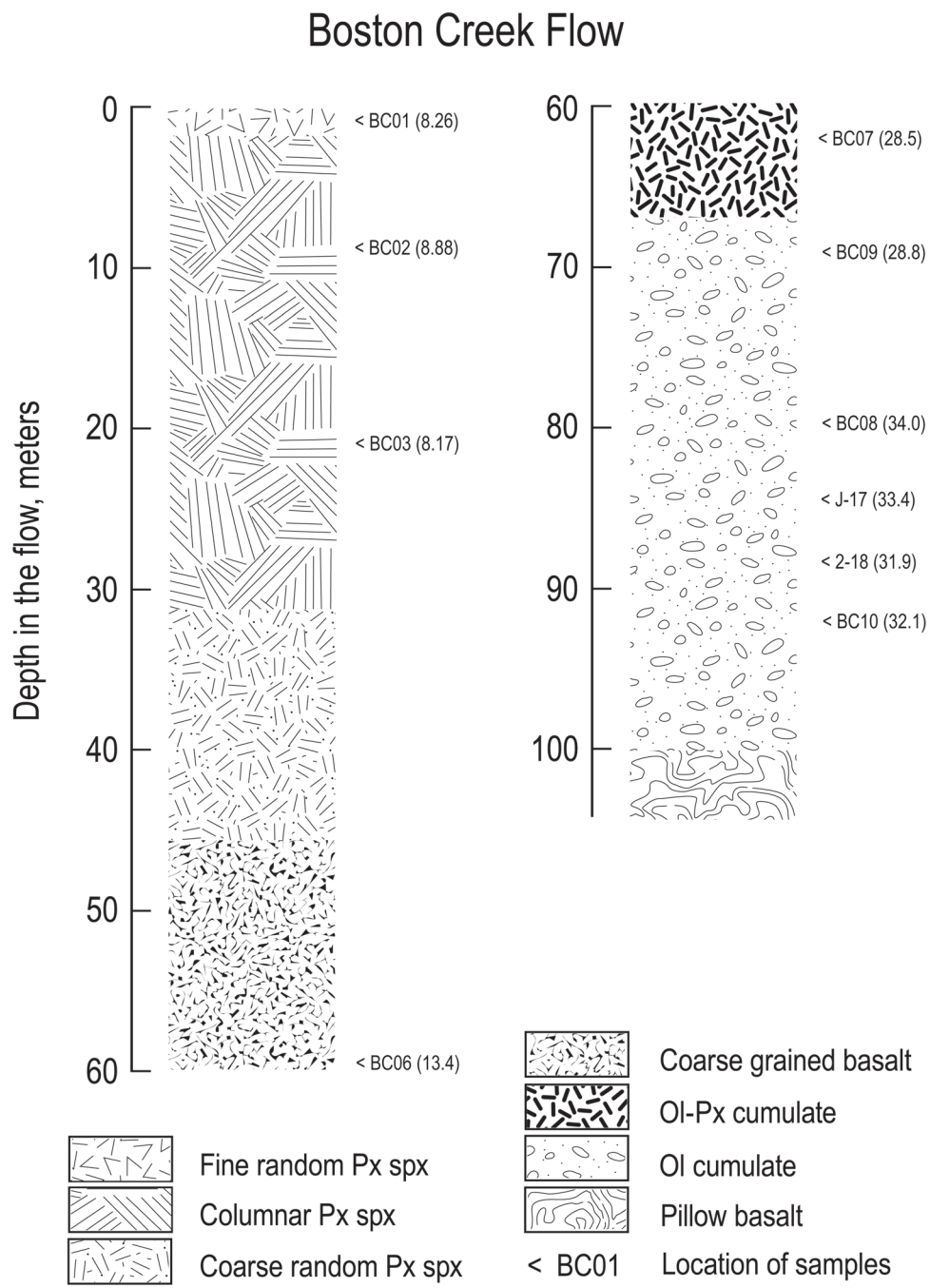
Sample	$^{147}\text{Sm}/^{144}\text{Nd}$	$\pm 2\text{SE}$	$^{143}\text{Nd}/^{144}\text{Nd}$	$\pm 2\text{SE}$	$\varepsilon^{143}\text{Nd}(\text{T})$	$\mu^{142}\text{Nd}$
BC01	0.1349	0.0007	0.511655	0.000001	+2.5	-4.4±1.9
BC02	0.1344	0.0007	0.511637	0.000001	+2.3	-1.9±2.0
Replicate*	0.1332	0.0007	0.511632	0.000001	+2.6	-3.8±1.5
BC03	0.1344	0.0007	0.511652	0.000001	+2.6	-1.0±1.7
Replicate*	0.1347	0.0007	0.511649	0.000002	+2.4	-1.9±3.5
BC06	0.1390	0.0007	0.511727	0.000001	+2.4	-5.6±2.1
Replicate*	0.1382	0.0007	0.511717	0.000001	+2.5	-3.8±1.6
BC08	0.1306	0.0007	0.511573	0.000001	+2.4	-5.5±2.2
Replicate*	0.1303	0.0007	0.511579	0.000001	+2.6	-2.0±2.5
BC09	0.1317	0.0007	0.511608	0.000001	+2.7	-6.1±2.1
Replicate*	0.1331	0.0007	0.511624	0.000001	+2.5	-4.6±2.1
BC10	0.1333	0.0007	0.511635	0.000001	+2.6	-5.5±1.7
Replicate*	0.1339	0.0007	0.511638	0.000001	+2.5	-4.4±2.8
J-17	0.1302	0.0007	0.511573	0.000001	+2.5	-5.3±2.1
2-18	0.1291	0.0006	0.511548	0.000001	+2.4	-1.9±2.0
BCR-1			0.512645	0.000002		+1.1±2.5
Replicate*			0.512645	0.000001		+0.3±1.7
Replicate*			0.512644	0.000002		+0.7±3.6

1526 Note. *Replicate digestions of the samples. The $^{147}\text{Sm}/^{144}\text{Nd}$ ratios were determined on ~3%
 1527 solution aliquots of the same sample digestions performed for the high-precision Nd isotopic
 1528 analyses, using the SA ICP-MS technique, as specified in the text. Due to the lack of
 1529 knowledge of the precise weight of the sample represented by the solution aliquots, only the
 1530 Sm/Nd ratios are reported here. Initial $\varepsilon^{143}\text{Nd}$ values were calculated for the age $T = 2720$ Ma
 1531 using the parameters specified in the text. The data for the USGS GRM BCR-1 were obtained
 1532 on three separate digestions over the course of the entire analytical campaign.
 1533

1534 **Table 8.** Lu-Hf isotope and concentration data for the Boston Creek komatiites

Sample	Lu (ppm)	Hf (ppm)	$^{176}\text{Lu}/^{177}\text{Hf}$	$\pm 2\text{SE}$	$^{176}\text{Hf}/^{177}\text{Hf}$	$\pm 2\text{SE}$	$\varepsilon^{176}\text{Hf(T)}$
BC02	0.2161	1.713	0.01790	0.00004	0.282069	0.000007	+3.6
BC03	0.2218	1.761	0.01787	0.00004	0.282077	0.000008	+4.0
BC06	0.2020	1.585	0.01809	0.00004	0.282094	0.000006	+4.2
BC08	0.05095	0.4189	0.01726	0.00003	0.282064	0.000018	+4.6
BC09	0.08686	0.6903	0.01786	0.00004	0.282098	0.000008	+4.7
BC10	0.05915	0.4195	0.02001	0.00004	0.282188	0.000014	+4.0

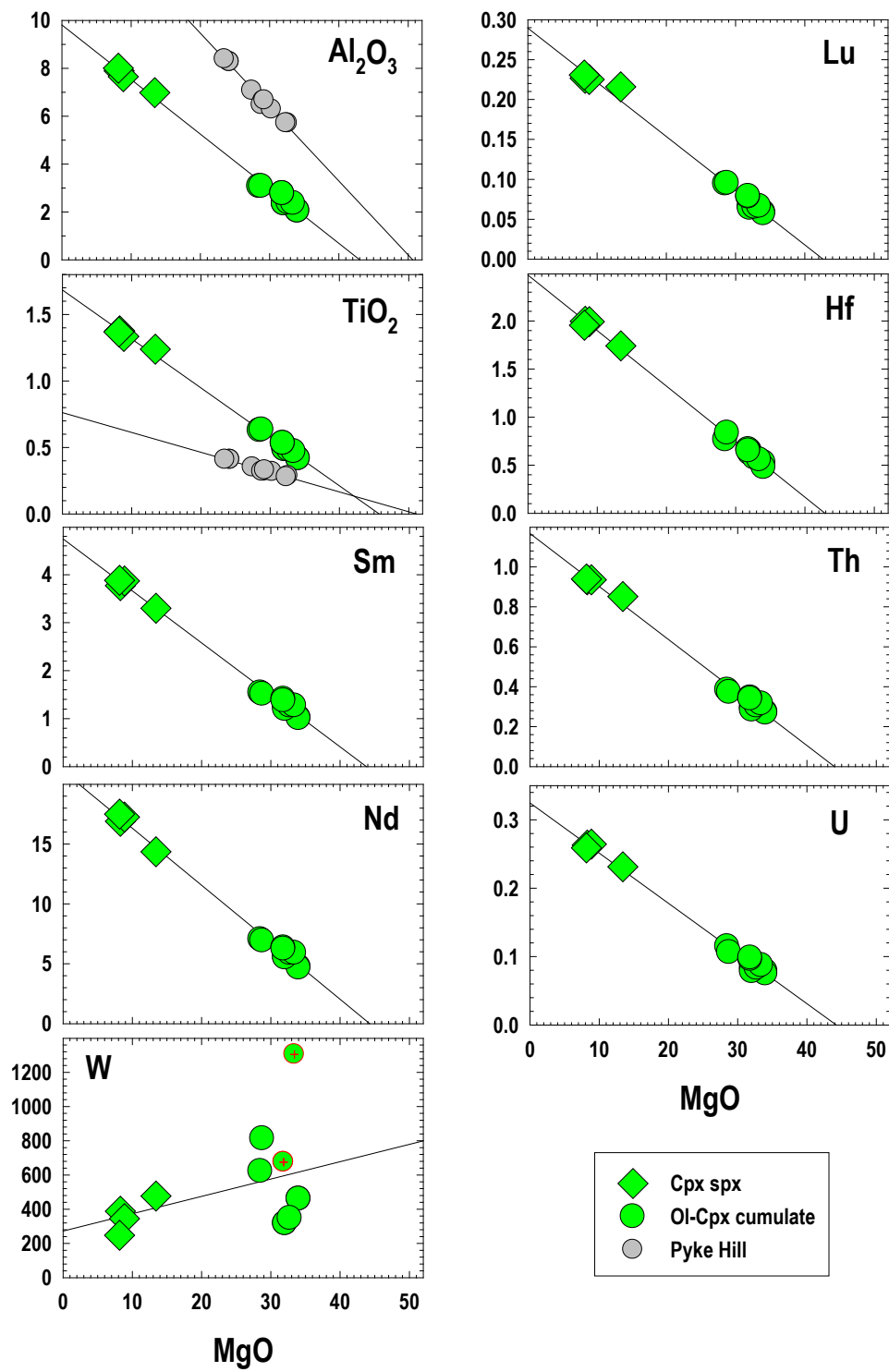
1535 Note. Initial $\varepsilon^{176}\text{Hf}$ values were calculated for the age $T = 2720$ Ma, using the parameters
 1536 specified in the text.
 1537

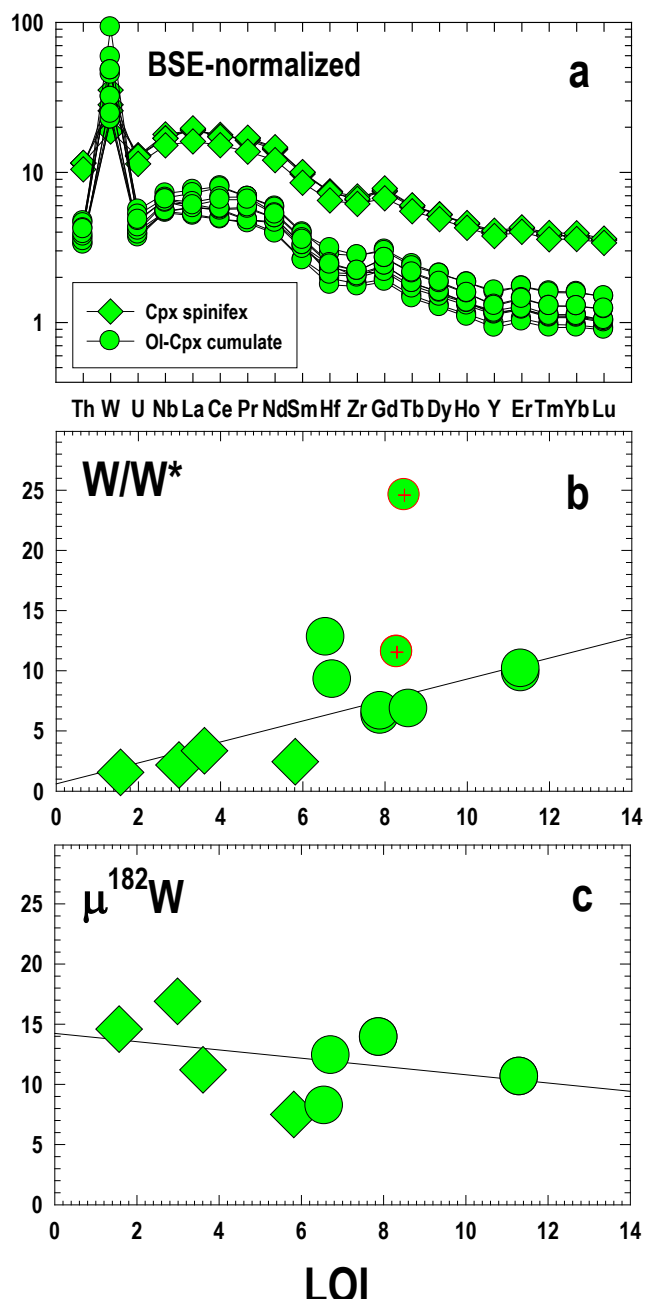


1538

1539 **Fig. 1.**

1540

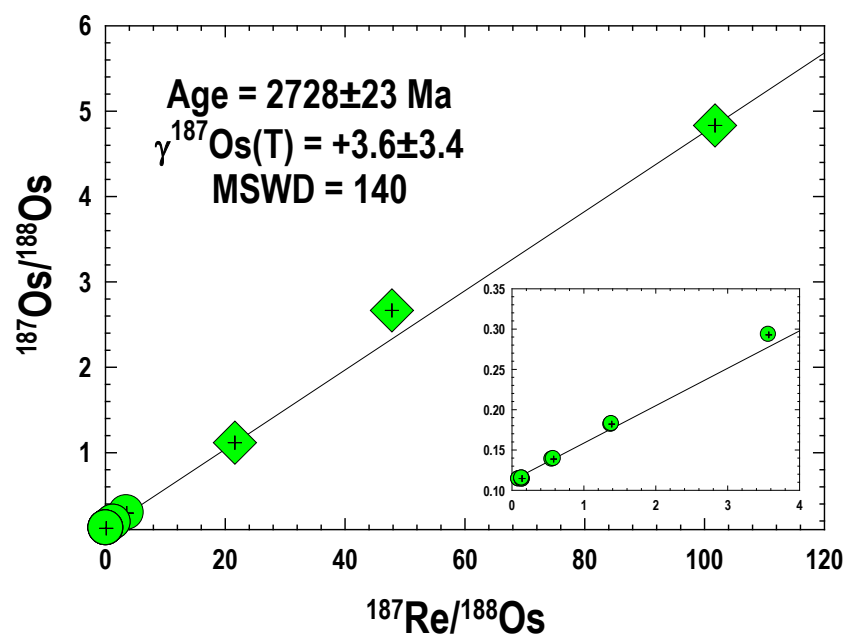




1544

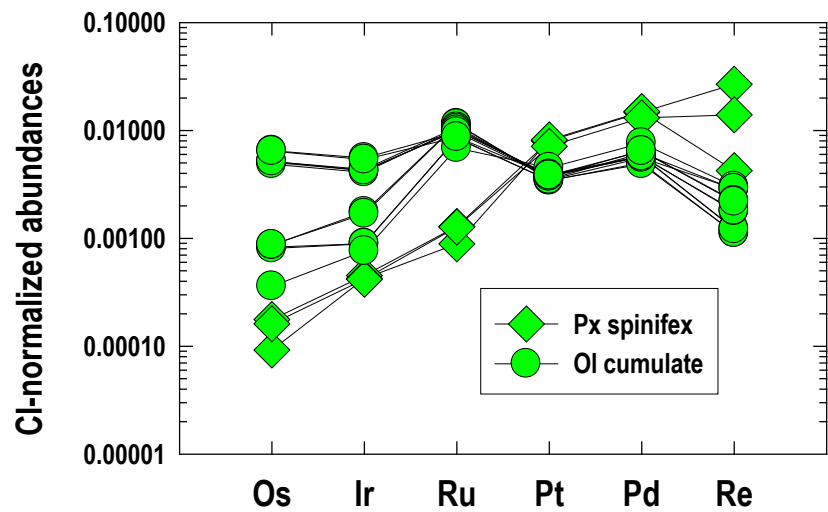
1545 Fig. 3.

1546



1547
 1548
 1549
 1550

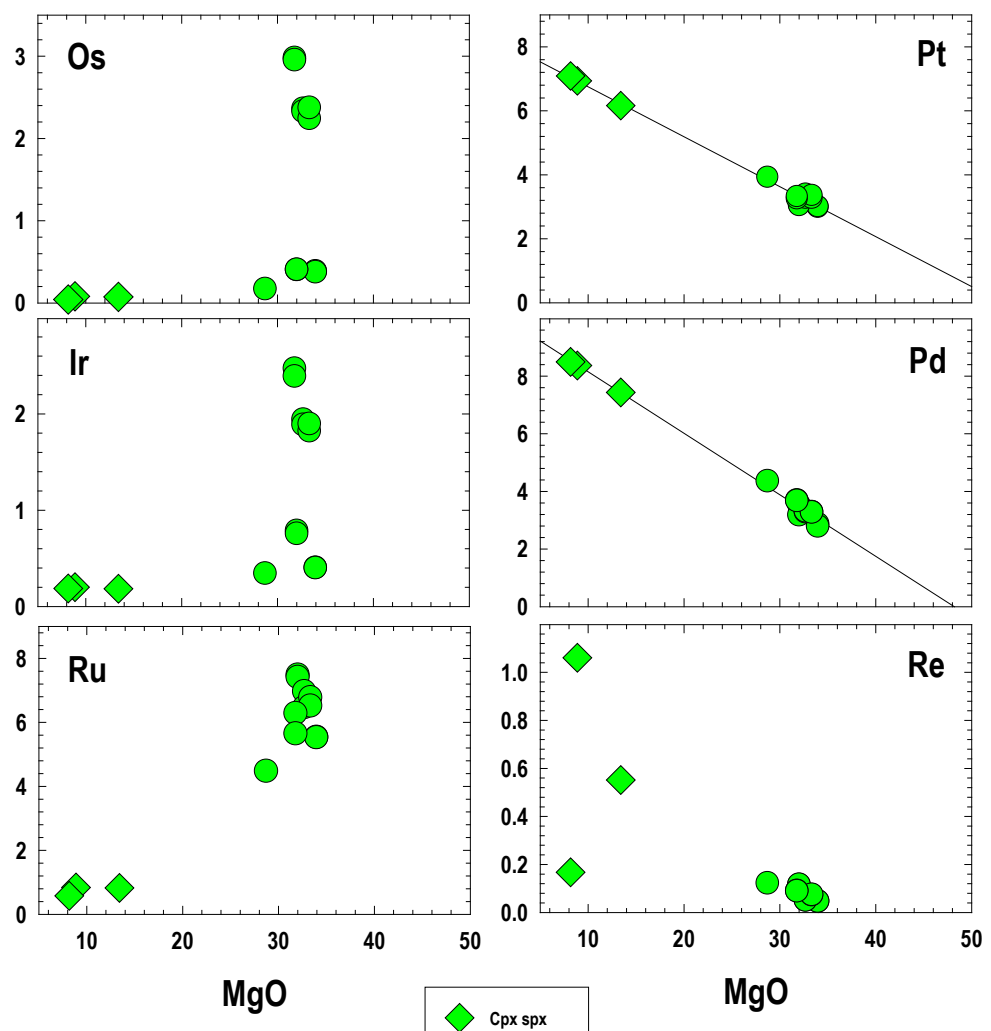
Fig. 4.



1551
1552

Fig. 5.

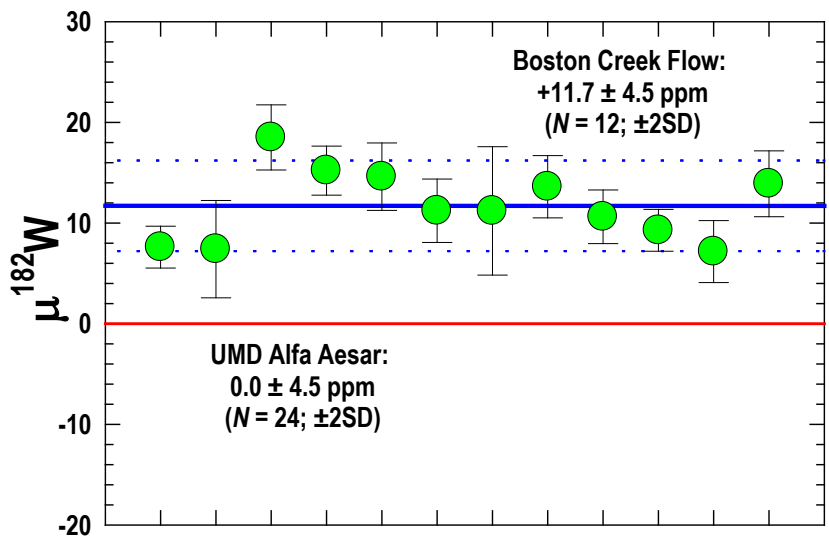
1553



1554

1555 Fig. 6.

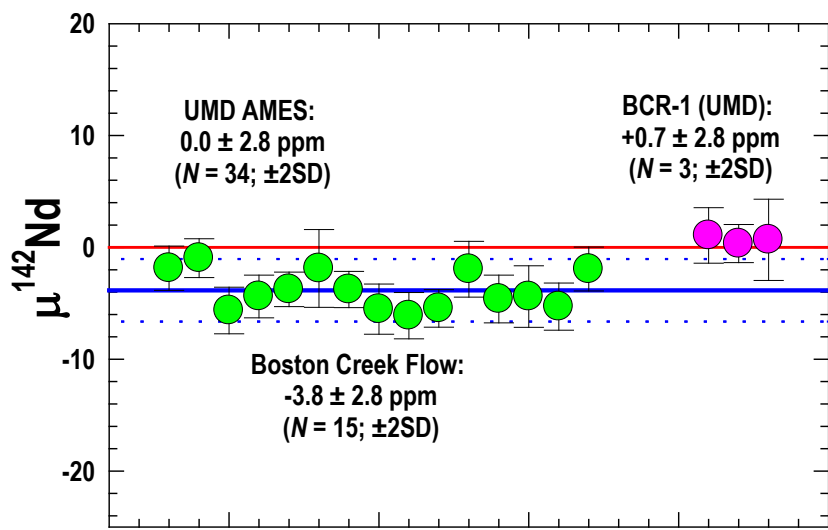
1556



1557

1558 **Fig. 7.**

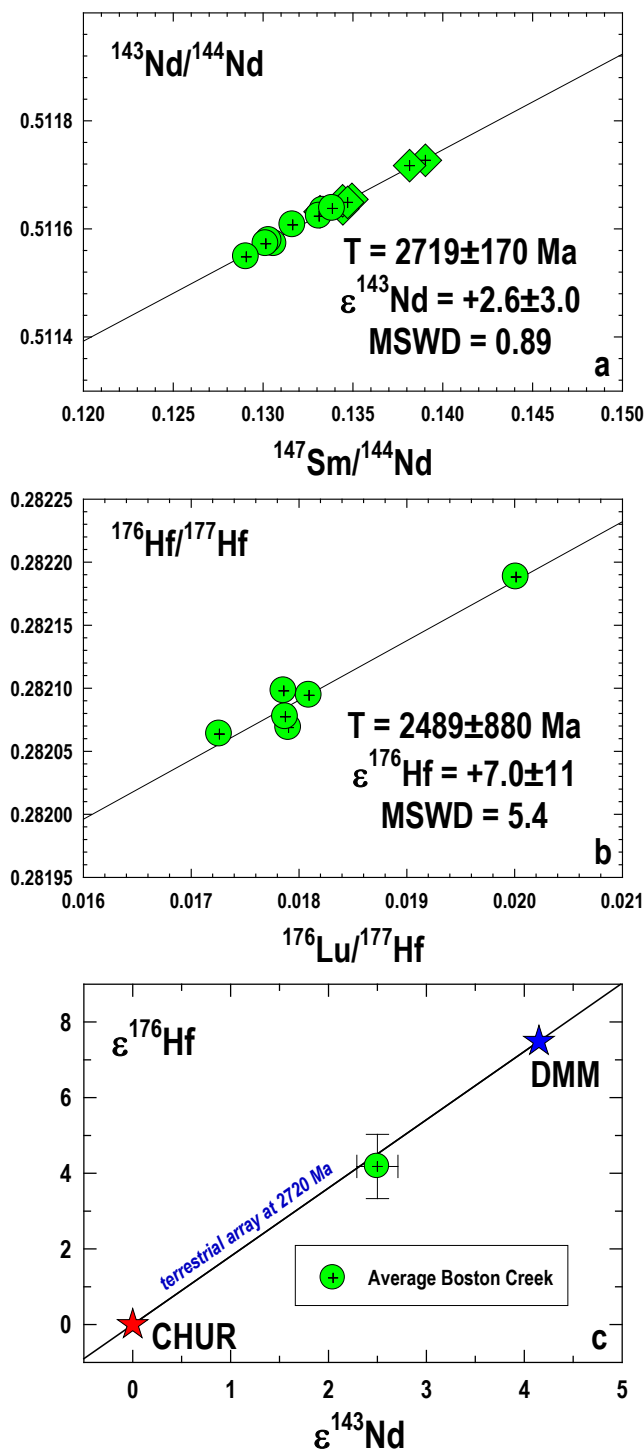
1559



1560

1561 **Fig. 8.**

1562

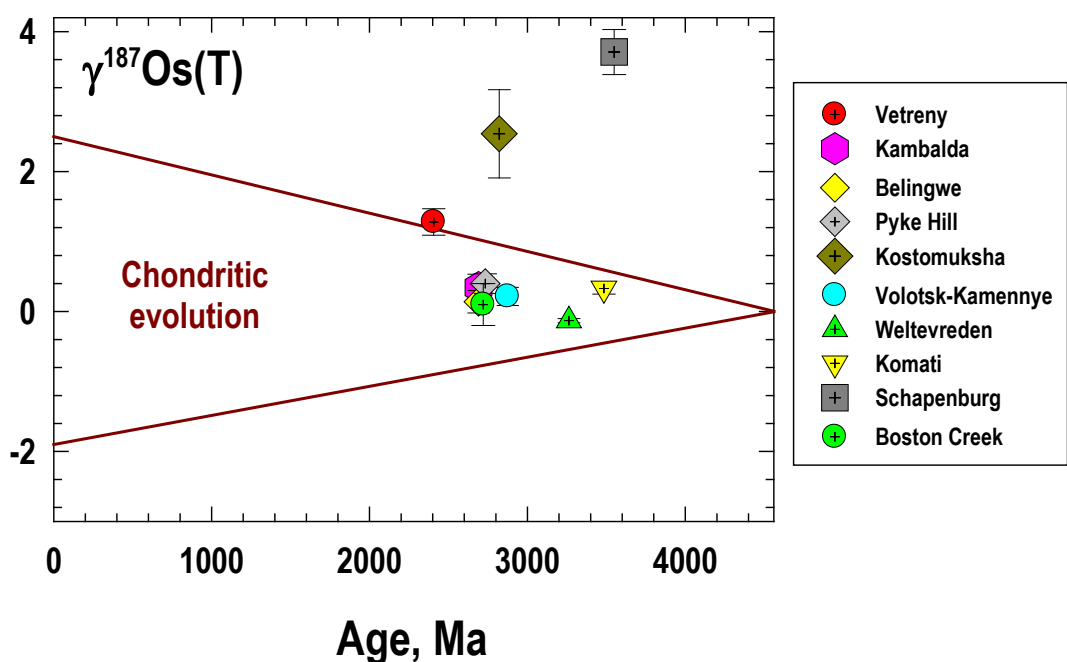


1563

1564

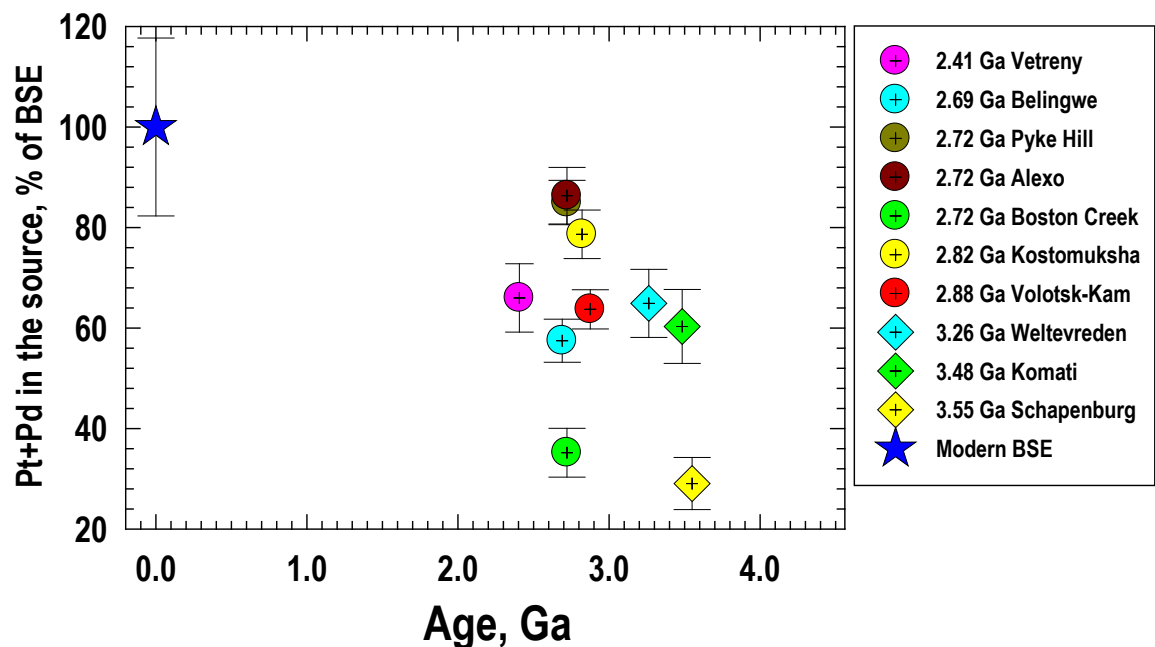
Fig. 9.

1565



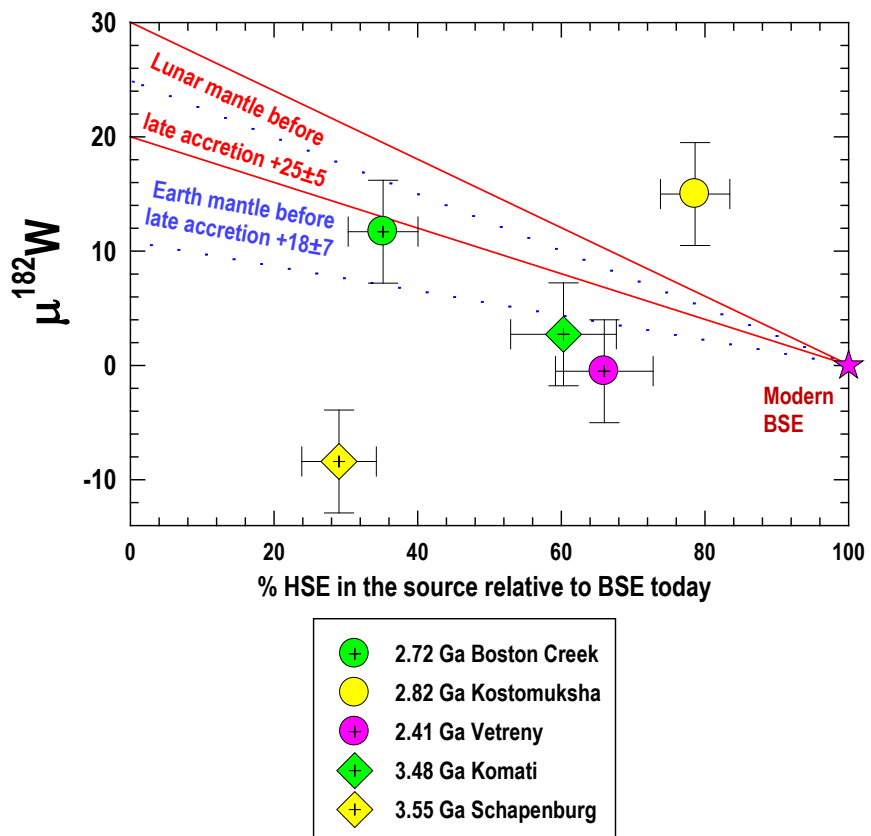
1566
1567
1568

Fig. 10.



1569
1570
1571

Fig. 11.



1572
1573
1574

Fig. 12.